Spin Dynamics in Adiabatic Transport through Quantum Dots

Bachelor Thesis

by

Claudius Hubig
(325249)

submitted

3 July 2012

First marker

Prof. Dr. Tobias Brandes

Second marker

Prof. Dr. Andreas Knorr

Supervisor

Dipl.-Phys. Anja Metelmann

Deutschsprachige Zusammenfassung

Die vorliegende Arbeit untersucht die Dynamik eines Systems bestehend aus einem Quantenpunkt mit einem Energieniveau, der an zwei externe Elektronenbäder sowie anisotropisch an einen externen, als groß angenommenen, Spin $\hat{J}$ gekoppelt ist. Der große Spin und der Quantenpunkt werden von einem homogenen, konstanten Magnetfeld B_z beeinflusst.

Wir leiten Bewegungsgleichungen für die Erwartungswerte der Komponenten von $\hat{J}$ im Rahmen einer Mean-Field-Approximation her.

Zur Herleitung der Erwartungswerte der Spinkomponenten im Quantenpunkt werden Keldysh-Greenfunktionen mit einer adiabatischen Näherung verwendet. Diese ermöglichen die Untersuchung endlicher Potentialdifferenzen zwischen den beiden Bädern.

Die resultierenden Gleichungen werden analytisch und numerisch ausgewertet. Dabei werden im Fall einer unendlichen Potentialdifferenz Ergebnisse ähnlich jenen von C. Monís et. al. [1] erreicht, jedoch tritt durch die adiabatische Näherung kein chaotisches Verhalten auf. Im Falle endlicher Potentialdifferenzen nimmt das System in Abhängigkeit vom Magnetfeld B_z und den Tunnelraten Γ teilweise vorher nicht beobachtete stationäre Zustände an.

Erklärung über die selbstständige Anfertigung der Arbeit

Hiermit erkläre ich an Eides statt, dass ich die vorliegende Arbeit selbstständig und eigenhändig sowie ausschließlich unter Verwendung der aufgeführten Quellen und Hilfsmittel angefertigt habe.

Berlin, den 2. Juli 2012

.....

Claudius Hubig

Contents

1. Introduction

During the last two decades, experimental verification of theoretical predictions about the dynamics of nanostructures has become a viable possibility [2–6]. This lead to an increase in research, especially regarding the highly quantised single- or few-electron dynamics in such structures, including both transport [7–9] and quantum computing [10, 11].

Chaotic behaviour [12, 13] has been found in closed systems [14, 15], where few electronic levels interact while influenced by external magnetic fields. Additionally, recent work shows that chaotic [1] or nonlinear [16, 17] dynamics also occur in open systems, consisting of one or more quantum dots coupled to electronic reservoirs. These systems share a common feature in addition to the homogeneous and constant magnetic field previously discussed in closed systems, namely a large spin.

Models including such large spins coupled to the quantum dot(s) describe various systems, some of which have applications in quantum computing or related fields [18, 19]. A typical example for transport through a quantum dot coupled to a large spin is that of a single molecule or atom acting as a link between two leads, where the nuclear spin of the atom or the combined nuclei spins of the molecule are non-negligible.

While it is possible to apply the equation of motion technique to the problem of electron tunnelling through a quantum dot in the infinite bias regime, it was also shown [20, 21] that the use of Keldysh Green's functions allows the systematic treatment of the finite bias regime. Furthermore, this approach is non-perturbative in the coupling to the leads. A detrimental aside is the complexity of calculations required to include non-adiabatic correction terms in the Keldysh Green's function approach.

This work investigates the model already researched by [1], but instead of the equation of motion technique, we use Keldysh Green's functions with an adiabatic approximation.

The system consists of a single-level quantum dot, coupled to two external leads, which are assumed to be in equilibrium. To account for possibly spin-polarised leads (due to a ferromagnetic structure, for example), we consider spin- and lead-dependent tunnelling rates. The 'nucleus spin' of the quantum dot is modelled by a large spin, where the coupling between electron spins in the quantum dot and the large spin is not necessarily isotropic. Finally, a homogeneous, constant magnetic field is applied to both the large spin and the electrons in the quantum dot.

The structure of this text is as follows: We start by introducing the model and the Hamiltonian and derive equations of motions for the large spin, using some basic approximations (Section 2). We continue by deriving Keldysh Green's functions for the electron spin components in the quantum dot and utilise these to obtain expressions for the expectation values of the electron spin components as well as the current through the quantum dot (Section 3). Afterwards, we assume an infinite bias and categorise the parameter space with the help of fixed

points (Section 4). Using the previously defined regions in parameter space, we investigate the finite bias regime (Section 5) and close with a conclusion (Section 6).

2. Model

We examine a quantum dot (QD) with a single energy level ε_{Dot} coupled to two external leads and a large spin $\hat{J}$ (cf. Fig. 1). An external magnetic field B_z is applied to the large spin and the QD, splitting the single energy level of the QD into two energy levels $\varepsilon_{\text{Dot}} \pm \frac{1}{2}B_z$.

Each of the leads $\alpha = \{\text{L(eft)}, \text{R(ight)}\}$ is assumed to be in equilibrium, described by Fermi functions f_α and chemical potentials μ_α. To account for spin-polarisation within the leads, we assume the tunnelling rates between the leads and the QD to depend on both the spin and the lead, i.e. $\Gamma_{\alpha\sigma}$.

To simplify the parameter space, we assume a symmetric bias. Hence, we introduce $\mu \equiv \mu_L$, $\mu_L = -\mu_R$.

The coupling between the large spin $\hat{J}$ and the electron spin components in the QD is not necessarily isotropic, we therefore introduce coupling coefficients λ_i, $i = \{x, y, z\}$, for the coupling between the i-th component of the large spin and the i-the component of the electron spin in the QD. Overall, this model is identical to the model examined by [1].

2.1. Hamiltonian

The Hamiltonian of the system described by Fig. 1 consists of three parts:

$$\hat{H} = \hat{H}_{\text{FA}} + \hat{H}_J + \hat{H}_{SJ}, \tag{2.1.1}$$

where $\hat{H}_{\text{FA}}$ denotes the Fano-Anderson Hamiltonian [22, 23]

$$\hat{H}_{\text{FA}} = \sum_{k\alpha\sigma} \varepsilon_{k\alpha\sigma} c^\dagger_{k\alpha\sigma} c_{k\alpha\sigma} + \sum_\sigma \tilde{\varepsilon}_\sigma d^\dagger_\sigma d_\sigma + \sum_{k\alpha\sigma} \left(V_{k\alpha\sigma} c^\dagger_{k\alpha\sigma} d_\sigma + V^\star_{k\alpha\sigma} d^\dagger_\sigma c_{k\alpha\sigma} \right), \tag{2.1.2}$$

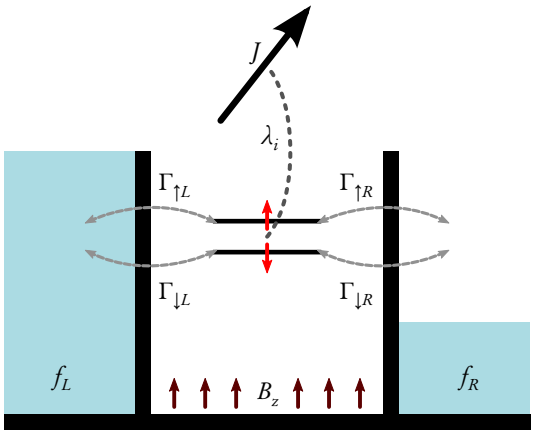

Figure 1: The model examined in this work. Two external leads are coupled to a quantum dot (QD) by tunnelling rates $\Gamma_{\alpha\sigma}$, depending on both the lead and the spin of the tunnelling electron. The spin components in the QD are coupled to a large external spin $\hat{J}$ by coupling coefficients λ_i. A homogeneous magnetic field B_z is applied to both the QD and the large spin.

with lead creation (annihilation) operators $c^\dagger_{k\alpha\sigma}$ ($c_{k\alpha\sigma}$), dot creation (annihilation) operators $d^\dagger_\sigma$ (d_σ), tunnelling amplitudes $V^{(*)}_{k\alpha\sigma}$ between lead α and the QD, energies $\varepsilon_{k\alpha\sigma}$ in lead α and the energy of an electron with spin σ in the QD given by $\tilde{\varepsilon}_\sigma = \varepsilon_{\mathrm{Dot}} \pm_\sigma \frac{1}{2}B_z$.

$\hat{H}_J$ describes the energy of the large spin J in the external magnetic field:

$$\hat{H}_J = B_z \hat{J}_z, \tag{2.1.3}$$

whereas $\hat{H}_{SJ}$ denotes the interaction between the electron spin in the QD, described by $\hat{S}$, and the large spin $\hat{J}$:

$$\hat{H}_{SJ} = \sum_{i=x,y,z} \lambda_i \hat{S}_i \hat{J}_i. \tag{2.1.4}$$

Focusing on the model already investigated by [1], we set $\lambda_{x,z} \equiv \lambda$, $\lambda_y \equiv 0$, corresponding to anisotropic coupling. Anisotropy in connection with quantum dots has been observed in various experiments [3, 24] and is a common factor in theoretical models that predict chaotic dynamics [25, 26].

2.2. Mean Field Approximation

The following derivation of equations of motion is based on the assumption that fluctuations $\delta\hat{J}_i$ of the large spin components $\hat{J}_i$ are small in comparison to the expectation values $\left\langle \hat{J}_i \right\rangle$. This assumption is perfectly valid in the classical limit $J^2 \to \infty$, but otherwise remains an approximation.

However, using this assumption and neglecting terms proportional to fluctuations of both the large and electron spin components (see Section A.1 for details), we are able to apply a mean field approximation and rewrite $\hat{H}_{SJ}$ in a semiclassical approximation as follows:

$$\hat{H}^{\mathrm{MF}}_{SJ} = \sum_{i=x,z} \lambda \left(\left\langle \hat{S}_i \right\rangle \hat{J}_i + \hat{S}_i \left\langle \hat{J}_i \right\rangle - \left\langle \hat{S}_i \right\rangle \left\langle \hat{J}_i \right\rangle \right). \tag{2.2.1}$$

2.3. Equations of Motion

After applying the mean field approximation, the equations of motion for the expectation values of the large spin components $\left\langle \hat{J}_i \right\rangle$ can be derived. Starting with the Heisenberg equation of motion

$$\left\langle \dot{\hat{J}}_k \right\rangle = -i \left\langle \left[\hat{J}_k, \hat{H}^{\mathrm{MF}} \right] \right\rangle + \left\langle \frac{\partial \hat{J}_k}{\partial t} \right\rangle, \tag{2.3.1}$$

where $[A, B]$ denotes the commutator of A and B, $\dot{A}$ signifies the total time derivative of A and we set $\hbar \equiv 1$, we then use (cf. Section A.2):

$$\left\langle \left[\hat{J}_k, \hat{H}^{\mathrm{MF}} \right] \right\rangle = B_z \left[\hat{J}_k, \hat{J}_z \right] + \lambda \left[\hat{J}_k, \left\langle \hat{S}_x \right\rangle \hat{J}_x + \left\langle \hat{S}_z \right\rangle \hat{J}_z \right], \tag{2.3.2}$$

and arrive at

$$\left\langle \dot{\hat{J}}_x \right\rangle = \left\langle \hat{J}_y \right\rangle \left(\lambda \left\langle \hat{S}_z \right\rangle + B_z \right), \tag{2.3.3}$$

$$\left\langle \dot{\hat{J}}_y \right\rangle = \left\langle \hat{J}_x \right\rangle \left(\lambda \left\langle \hat{S}_z \right\rangle + B_z \right) - \lambda \left\langle \hat{S}_x \right\rangle \left\langle \hat{J}_z \right\rangle, \tag{2.3.4}$$

$$\left\langle \dot{\hat{J}}_z \right\rangle = \left\langle \hat{J}_y \right\rangle \lambda \left\langle \hat{S}_x \right\rangle. \tag{2.3.5}$$

3. Electronic Green's Functions

Keldysh Green's functions are used to derive the expectation values of the QD spin operators $\left\langle \hat{S}_i \right\rangle$. To this end, we define retarded lead Green's functions $g^R_{k\alpha\sigma,l\beta\tau}$, retarded tunnelling Green's functions $G^R_{k\alpha\sigma,\tau}$ and retarded dot Green's functions $G^R_{\sigma,\tau}$ as follows [21]:

$$g^R_{k\alpha\sigma,n}(t,t') \equiv -i\theta(t-t') \left\langle \left\{ c_{k\alpha\sigma}(t), c^\dagger_{l\beta\tau}(t') \right\} \right\rangle, \tag{3.0.6}$$

$$G^R_{k\alpha\sigma,\tau}(t,t') \equiv -i\theta(t-t') \left\langle \left\{ c_{k\alpha\sigma}(t), d^\dagger_\tau(t') \right\} \right\rangle, \tag{3.0.7}$$

$$G^R_{\sigma,\tau}(t,t') \equiv -i\theta(t-t') \left\langle \left\{ d_\sigma(t), d^\dagger_\tau(t') \right\} \right\rangle. \tag{3.0.8}$$

Here, g^R denotes the undisturbed retarded Green's function in the leads. Therefore, to calculate g^R, we set $V^{(\star)}_{k\alpha\sigma} \equiv 0$.

The adiabatic approximation is then implemented by taking $t' \equiv 0$ as well as neglecting the time-dependence of $\hat{J}_i$ with regard to these expectation values. These approximations are based on the assumption that the time evolution of the electron spin within the QD occurs on a much smaller time scale than the long-term evolution of the large spin. This assumption neglects effects caused by short-lived displacements or fluctuations of the electron spin $\hat{S}$ and assumes that the effective time evolution solely depends on the large spin $\hat{J}$.

3.1. Dyson Equation

Using the Heisenberg equation of motion for the annihilation operators in Eq. (3.0.6) – (3.0.8), an equation of motion for $G^R_{\sigma,\tau}(t)$ can be derived, cf. Section A.3. Applying a Fourier transformation to this equation yields the following Dyson equation:

$$\delta_{\sigma,\tau} = \left(\omega - \varepsilon_\sigma\right) G^R_{\sigma,\tau}(\omega) - \frac{\lambda}{2} \left\langle \hat{J}_x \right\rangle G^R_{-\sigma,\tau}(\omega) - \sum_{k\alpha} \left| V_{k\alpha\sigma} \right|^2 g^R_{k\alpha\sigma,k\alpha\sigma}(\omega) G^R_{\sigma,\tau}(\omega), \tag{3.1.1}$$

$$\varepsilon_\sigma \equiv \varepsilon_{\mathrm{Dot}} \pm_\sigma \frac{1}{2} \left(B_z + \lambda \left\langle \hat{J}_z \right\rangle \right), \tag{3.1.2}$$

where $-\sigma$ denotes the spin state anti-parallel to σ, i.e. $\sigma = \uparrow \Rightarrow -\sigma = \downarrow$.

It is then possible to identify the retarded self-energy $\Sigma^R_{\alpha\sigma}$ for spin σ in lead α:

$$\Sigma^R_\sigma \equiv \sum_\alpha \Sigma^R_{\alpha\sigma} \tag{3.1.3}$$

$$= \sum_{k\alpha} \left| V_{k\alpha\sigma} \right|^2 g^R_{k\alpha\sigma,k\alpha\sigma}(\omega) \tag{3.1.4}$$

$$= \sum_\alpha \left(\frac{1}{2}\Lambda_{\alpha\sigma}(\omega) - \frac{i}{2}\Gamma_{\alpha\sigma}(\omega) \right) \tag{3.1.5}$$

$$\approx -\frac{i}{2}\sum_\alpha \Gamma_{\alpha\sigma}. \tag{3.1.6}$$

Approximation (3.1.6) is identical to a flat band approximation. Additionally, we set $\varepsilon_{\mathrm{Dot}} \equiv \Lambda_{\alpha\sigma} \equiv 0$ from now on, as these only effect a constant shift of the dot energy in relation to the chemical potentials of the leads.

Eq. (3.1.1) then yields four algebraic equations for $G^R_{\sigma,\tau}$ with $\{\sigma,\tau\} = \uparrow,\downarrow$. These equations can be solved easily and result in expressions for $G^R_{\sigma,\tau}(\omega)$, cf. Eq. (A.3.13) – (A.3.16).

3.2. Electron Spin in the Quantum Dot

To calculate $\left\langle \hat{S}_i \right\rangle$, we use the lesser dot Green's function defined as [21]:

$$G^<_{\sigma,\tau}(t) \equiv i \left\langle d^\dagger_\tau d_\sigma(t) \right\rangle. \tag{3.2.1}$$

It is related to G^R via the Keldysh equation [21]:

$$\boldsymbol{G}^< = \boldsymbol{G}^R \boldsymbol{\Sigma}^< \boldsymbol{G}^A, \tag{3.2.2}$$

which is a matrix equation in $\mathbb{C}^2$ spin space. The diagonal elements of the lesser self-energy are given by

$$\Sigma^<_\sigma = \sum_{k\alpha} |V_{k\alpha\sigma}|^2 g^<_{k\alpha\sigma,k\alpha\sigma}(\omega) \tag{3.2.3}$$

$$= i \left(\sum_\alpha f_\alpha(\omega)\Gamma_{\alpha\sigma} \right). \tag{3.2.4}$$

With $G^<$, the following expressions for $\left\langle \hat{S}_i \right\rangle$ can be derived (cf. Section A.3.4):

$$\left\langle \hat{S}_x \right\rangle = \frac{\lambda \left\langle \hat{J}_x \right\rangle}{2} \int \frac{\mathrm{d}\omega}{2\pi} \sum_{\alpha\sigma} \left\{ f_\alpha(\omega)\Gamma_{\alpha\sigma} \frac{\left(\omega + \varepsilon_\sigma\right)}{N(\omega)} \right\}, \tag{3.2.5}$$

$$\left\langle \hat{S}_y \right\rangle = \frac{-\lambda \left\langle \hat{J}_x \right\rangle}{4} \int \frac{\mathrm{d}\omega}{2\pi} \sum_{\alpha\sigma} \left\{ \pm_\sigma f_\alpha(\omega)\Gamma_{\alpha\sigma}\Gamma_{-\sigma} \frac{1}{N(\omega)} \right\}, \tag{3.2.6}$$

$$\left\langle \hat{S}_z \right\rangle = \frac{1}{2} \int \frac{\mathrm{d}\omega}{2\pi} \sum_{\alpha\sigma} \left\{ \pm_\sigma f_\alpha(\omega) \Gamma_{\alpha\sigma} \left((\omega + \varepsilon_\sigma)^2 + \frac{\Gamma_{-\sigma}^2}{4} - \frac{\lambda^2}{4} \left\langle \hat{J}_x \right\rangle^2 \right) \frac{1}{N(\omega)} \right\}, \tag{3.2.7}$$

$$N(\omega) \equiv \left| (\omega + \varepsilon_\uparrow + \Gamma_\downarrow)(\omega + \varepsilon_\downarrow + \Gamma_\uparrow) - \frac{\lambda^2}{4} \left\langle \hat{J}_x \right\rangle^2 \right|^2. \tag{3.2.8}$$

It is possible to solve these integrals analytically, provided that $T \equiv 0$, i.e.

$$f_\alpha(\omega) = \theta(\mu_\alpha - \omega), \tag{3.2.9}$$

by using Mathematica 8 and its analytic `Integrate[]` function. To reach conformance with numeric results, it is furthermore necessary to introduce a piecewise definition of specific arctan() terms, because their arguments show poles with sign conversions. An exemplary expression for $\left\langle \hat{S}_z \right\rangle$ can be found in Eq. (A.3.21).

These analytic expressions are highly nonlinear, making it (practically) impossible to find analytic roots, which are a prerequisite for the fixed point analysis. Furthermore, analytic evaluation is only slightly faster than numeric integration. We therefore disregard these results for now and concentrate on numeric approaches.

However, in Section 5, we will use these expressions, and the analytic derivatives thereof, during the calculation of Jacobians at specific fixed points. As the reader may imagine, the arising terms lose neither complexity nor length.

3.3. Current through the Quantum Dot

In this section, we will roughly follow Section 12.4 in [21], as the general strategy and starting point presented there are nearly identical to ours.

It is possible to express the current I_α from lead α into the QD as the time-derivative of the number operator in lead α, namely:

$$I_\alpha \equiv -e \langle \dot{n}_\alpha \rangle \tag{3.3.1}$$

$$= -ei \left[\hat{H}, \sum_{k\sigma} c_{k\alpha\sigma}^\dagger c_{k\alpha\sigma} \right] \tag{3.3.2}$$

$$= -ei \sum_{k\sigma} \left\{ V_{k\alpha\sigma}^\star \left\langle d_\sigma^\dagger c_{k\alpha\sigma} \right\rangle - V_{k\alpha\sigma} \left\langle c_{k\alpha\sigma}^\dagger d_\sigma \right\rangle \right\}. \tag{3.3.3}$$

Using the lesser tunnelling Green's function, which is defined analogous to the lesser dot Green's function, we can write this as

$$I_\alpha = -e \sum_{k\sigma} \left\{ V_{k\alpha\sigma}^\star G_{k\alpha\sigma,\sigma}^< - V_{k\alpha\sigma} G_{\sigma,k\alpha\sigma}^< \right\}. \tag{3.3.4}$$

The lesser tunnelling Green's function can be expressed via the contact and dot Green's function by the corresponding equation for the retarded tunnelling Green's function, Eq. (A.3.11), and employing the rules of analytic continuation [21], namely:

$$G^{<}_{k\alpha\sigma,\sigma} = V_{k\alpha\sigma}\left(g^{R}_{k\alpha\sigma}G^{<}_{\sigma,\sigma} + g^{<}_{k\alpha\sigma}G^{R}_{\sigma,\sigma}\right), \tag{3.3.5}$$

whereby the current I_α becomes

$$I_\alpha = -2e\sum_\sigma \int \frac{\mathrm{d}\omega}{2\pi}\Re\left\{\Sigma^{R}_{\alpha\sigma}G^{<}_{\sigma,\sigma} + \Sigma^{<}_{\alpha\sigma}G^{A}_{\sigma,\sigma}\right\}. \tag{3.3.6}$$

Eq. (3.3.6) coincides with the result reached by [21].

Substituting in the previous definitions of the lesser and retarded self-energy (Eq. (3.2.3) – (3.1.6)) and the lesser and advanced dot Green's function (cf. Section A.3.3, A.3.4) leads to:

$$I_\alpha = -e\sum_{\beta\sigma}\int \frac{\mathrm{d}\omega}{2\pi}\frac{\Gamma_{\alpha\sigma}}{N(\omega)}\left\{f_\beta(\omega)\left((\omega+\varepsilon_\sigma)^2\Gamma_{\beta\sigma} + \frac{\Gamma^2_{-\sigma}\Gamma_{\beta\sigma}}{2} + \frac{\lambda^2\left\langle\hat{J}_x\right\rangle^2}{4}\Gamma_{\beta,-\sigma}\right)\right.$$
$$\left. - f_\alpha(\omega)\left(\Gamma_{-\sigma}\left(\Gamma_\uparrow\Gamma_\downarrow + \lambda^2\left\langle\hat{J}_x\right\rangle^2\right) - (\omega+\varepsilon_\sigma)^2\Gamma_\sigma\right)\right\} \tag{3.3.7}$$

The first term corresponds to the occupation of both leads (hence the sum $\sum_\beta$) and the respective probabilities of tunnelling from the QD into one of the leads, while the second term describes the interaction between the lead in question (α) and the QD.

We should stress that I_α denotes the current *from* lead α into the QD and may well be negative; the sign of I_α carries the information about the direction of the current. For example, if $\mu_L < 0$ and $\mu_R > 0$, we have $I_L < 0$ and $I_R > 0$.

4. Infinite Bias Regime

In this section we assume an infinite bias, that is, $\mu \to \infty$. To further simplify the results and aid in the comparison with previous results by [1], we set $\Gamma \equiv \Gamma_\uparrow \equiv \Gamma_\downarrow$, $\Gamma_{L\uparrow} \equiv \Gamma_{R\uparrow}$, $\Gamma_{R\downarrow} \equiv 0$.

With these assumptions, spin down electrons can only tunnel into the QD from the left lead, and a spin flip within the QD has to take place before they can leave the QD to the right. We thereby describe spin-polarised leads, but instead of modelling this polarisation by spin-dependent Fermi functions, we describe the effect of spin-polarisation on the system by spin-dependent tunnelling rates. Ferromagnetic leads are a prominent example of spin-polarised leads.

With the assumption of an infinite bias, the Fermi functions in the leads become either 0 or 1:

$$f_\alpha\Big|_{\mu\to\infty} = \delta_{\alpha,L}. \tag{4.0.8}$$

Employing the residue theorem, the equations for $\left\langle \hat{S}_i \right\rangle$ (Eq. (3.2.5) – (3.2.7)) result in the following expressions:

$$\left\langle \hat{S}_x \right\rangle = -\frac{\lambda \left\langle \hat{J}_x \right\rangle \varepsilon_\uparrow}{2\left(\lambda^2 \left\langle \hat{J}_x \right\rangle^2 + \Gamma^2 + 4\varepsilon_\uparrow^2\right)}, \tag{4.0.9}$$

$$\left\langle \hat{S}_y \right\rangle = \frac{\lambda \left\langle \hat{J}_x \right\rangle \Gamma}{4\left(\lambda^2 \left\langle \hat{J}_x \right\rangle^2 + \Gamma^2 + 4\varepsilon_\uparrow^2\right)}, \tag{4.0.10}$$

$$\left\langle \hat{S}_z \right\rangle = \frac{1}{4}\left(\frac{\lambda^2 \left\langle \hat{J}_x \right\rangle^2}{\lambda^2 \left\langle \hat{J}_x \right\rangle^2 + \Gamma^2 + 4\varepsilon_\uparrow^2} - 1\right). \tag{4.0.11}$$

Since we previously set $\varepsilon_{\text{Dot}} \equiv 0$, we now have $\varepsilon_\uparrow = -\varepsilon_\downarrow$ and are therefore able to solely use $\varepsilon_\uparrow$.

If we furthermore assume symmetric coupling to the leads, we reach

$$I_L = \frac{\Gamma e}{2\hbar} = -I_R, \tag{4.0.12}$$

which fits well with our expectations.

4.1. Fixed Points

By combining Eq. (4.0.9) – (4.0.11) with the equations of motion (Eq. (2.3.3) – (2.3.5)) and setting the time derivatives to zero, eight fixed points are found, two of which always have finite imaginary parts. Since it is physically impossible to attain these stationary states, we concentrate on the remaining six fixed points, which are identical to [1, Eq. 11a – c].

We therefore introduce the following, similar, notation:

$$\mathbf{P} = \left(\left\langle \hat{J}_x \right\rangle_0, \left\langle \hat{J}_y \right\rangle_0, \left\langle \hat{J}_z \right\rangle_0\right). \tag{4.1.1}$$

The six remaining fixed points[1] are then given by:

$$\mathbf{P}_\pm = (0, 0, \pm j), \tag{4.1.2}$$

$$\mathbf{P}_{\text{II}+\pm} = (\mathscr{A}, \pm\mathscr{B}, -B_z/\lambda), \tag{4.1.3}$$

[1] [1] referred to $\mathbf{P}_{\text{II}-\pm}$ and $\mathbf{P}_{\text{II}+\pm}$ as $\mathbf{P}_{\text{II},1\pm}$ and $\mathbf{P}_{\text{II},2\pm}$, respectively. However, since 1 and 2 denote the sign of $\left\langle \hat{J}_x \right\rangle$, the notation using + and − appears much more natural.

$$\mathbf{P}_{\mathrm{II}-\pm} = (-\mathscr{A}, \pm\mathscr{B}, -B_z/\lambda), \tag{4.1.4}$$

where these definitions have been used:

$$\mathscr{A} = \frac{\Gamma\sqrt{\lambda - 4B_z}}{2\lambda\sqrt{B_z}} \tag{4.1.5}$$

$$\mathscr{B} = \frac{\sqrt{4B_z\left(j^2\lambda^2 + \Gamma^2\right) - \Gamma^2\lambda^2 - 4B_z^3}}{2\lambda\sqrt{B_z}} \tag{4.1.6}$$

$$j = \sqrt{\left\langle \hat{J}_x \right\rangle^2 + \left\langle \hat{J}_y \right\rangle^2 + \left\langle \hat{J}_z \right\rangle^2}. \tag{4.1.7}$$

We note that the fixed points $\mathbf{P}_{\mathrm{II}}$[2] meet the requirements $\left\langle \hat{S}_x \right\rangle = 0$ and $\left\langle \hat{S}_z \right\rangle = -\frac{B_z}{\lambda}$, which result in stationary states of the equations of motion. These requirements are met by nearly all fixed points analysed in this work, with $\mathbf{P}_{\pm}$ being the only exceptions.

The physical existence of $\mathbf{P}_{\mathrm{II}}$ then depends on the imaginary parts of $\mathscr{A}$ and $\mathscr{B}$ to equal zero. Solving the equations $\mathscr{A} = 0 = \mathscr{B}$ leads to Fig. 2, which allows us to define *three regions* in parameter space.

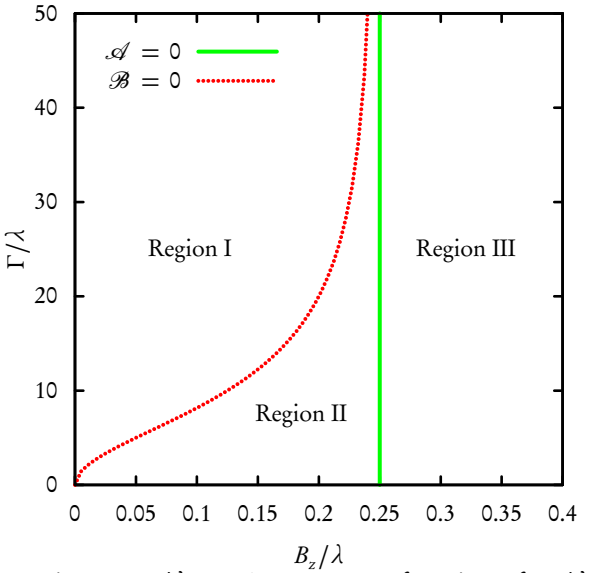

Figure 2: Γ/λ at $\mathscr{A}, \mathscr{B} = 0$ as a function of B_z/λ for $j \equiv 10$. $\mathscr{A} = 0$ is equivalent to $B_z = \frac{\lambda}{4}$, while $\mathscr{B} = 0$ depends on Γ as well as j [1, Fig. 2a].

4.2. Dynamics of the System

The equations of motion (Eq. (2.3.3) – (2.3.5)) can only be solved numerically. Therefore, a small C programme was written, using the GNU Scientific Library Version 1.15, to numerically integrate Eq. (3.2.5) – (3.2.7) and calculate solutions for Eq. (2.3.3) – (2.3.5).

By using the previously defined regions, a systematic treatment of the parameter space $(B_z/\lambda, \Gamma/\lambda)$ is possible. We ensure that the dynamics of systems within one region of the parameter space differ only quantitatively, not qualitatively, by testing different sets of parameters within each region and comparing the results. However, to ease comparison with the results obtained by [1] and avoid needless repetition, we will only present one set of parameters per region here.

[2] We will use $\mathbf{P}_{\mathrm{II}}$ to refer to $\mathbf{P}_{\mathrm{II}++}$, $\mathbf{P}_{\mathrm{II}--}$, $\mathbf{P}_{\mathrm{II}-+}$ and $\mathbf{P}_{\mathrm{II}+-}$.

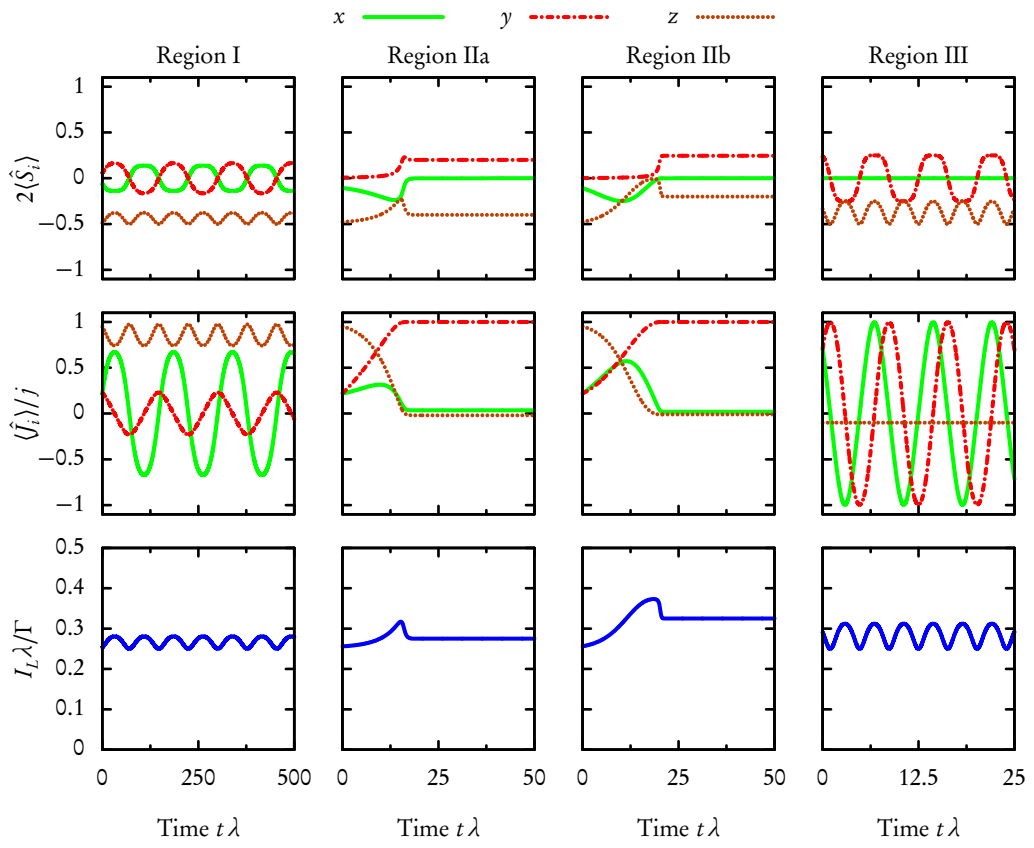

Figure 3: Behaviour of system in each of the three regions in the infinite bias regime. The parameters are as follows: region I: $B_z = 0.1\lambda$, $\Gamma = 9\lambda$, region IIa: $B_z = 0.2\lambda$, $\Gamma = 0.7\lambda$, region IIb: $B_z = 0.1\lambda$, $\Gamma = 0.16\lambda$, region III: $B_z = 1\lambda$, $\Gamma = 10\lambda$. Initial conditions: region I & II: $\left\langle\hat{J}_x(0)\right\rangle = \left\langle\hat{J}_y(0)\right\rangle = (5/\sqrt{2})(\sqrt{5}-1)/2$, $\left\langle\hat{J}_z(0)\right\rangle = (5/\sqrt{2})\sqrt{5+\sqrt{5}}$; region III: $\left\langle\hat{J}_x(0)\right\rangle = \left\langle\hat{J}_y(0)\right\rangle = 3\sqrt{6.5}$, $\left\langle\hat{J}_z(0)\right\rangle = -1$.

Fig. 3 illustrates the behaviour of the system in the infinite bias regime.

Region I and III are characterised by nearly-sinusoidal oscillations of the current, electron spin and large spin components. The dynamics are nearly identical to those observed previously [1], except for damping. This can easily be explained by the adiabatic approach used here: The adiabatic approximations employed to calculate the electronic Green's function for the QD only take into account the length of time evolution ($t' \equiv 0$); the assumption that $\left\langle\hat{J}_i\right\rangle$ does not depend on time nullifies any fluctuations in the dynamics of the electron spin, which would otherwise result in a loss of adiabacity and lead to damped dynamics.

Region II contains four more fixed points, denoted by $\mathbf{P}_{\mathrm{II}}$. Fig. 3 shows that at least one of these, $\mathbf{P}_{\mathrm{II}++}$, is attractive. Calculations with negative initial values for $\left\langle\hat{J}_x\right\rangle$ and $\left\langle\hat{J}_y\right\rangle$ show that $\mathbf{P}_{\mathrm{II}--}$ is also attractive, while $\mathbf{P}_{\mathrm{II}-+}$ and $\mathbf{P}_{\mathrm{II}+-}$ are repulsive.

Systems in this region enter a stationary state within a relatively short time. This time depends strongly on the initial values of $\left\langle \hat{J}_i \right\rangle$, but never exceeds a few oscillation periods of similar systems in region I or III.

Differing strongly from [1, Fig. 4], the system does not exhibit chaotic behaviour, nor do the dynamics of the system change considerably if the parameters are varied within region II; this allows us to concentrate on one set of parameters (region IIa in Fig. 3).

5. Finite Bias Regime

This section examines exemplary sets of parameters in each of the three regions defined by Fig. 2. Since, as noted previously, the dynamics exhibited by systems within one region are relatively uniform, it is sufficient to examine one system per region. Each section starts with a description of the behaviour observed and then continues with an analysis of the fixed points related to this behaviour.

The three parameters of interest in each region are: the symmetrical chemical potential μ, which is equal to the potential in the left lead and half the applied bias: $\mu = \mu_L$, $V_{\text{Bias}} = 2\mu$, the magnetic field B_z in relation to the coupling constant λ and the tunnelling rate Γ in relation to the coupling constant λ.

5.1. Region I

Region I is characterised by $B_z < \frac{\lambda}{4}$ and relatively high values of Γ/λ. In this section, we set $B_z \equiv 0.1\lambda$ and $\Gamma \equiv 9\lambda$.

5.1.1. Dynamics of the System

From Fig. 4, we identify four different *zones* within region I as a function of the chemical potential μ. The transition from zone i to zone j occurs at a specific potential μ_{ij}. In the system analysed here, these potentials are as follows: $\mu_{01} \approx -5$, $\mu_{12} \approx 7.2$, $\mu_{23} \approx 60.2$. The initial values of $\left\langle \hat{J}_i \right\rangle$ have a slight, but negligible, effect on the exact values of μ_{ij}.

Since μ_{01} is negative (negative detuning), we also observe negative currents I_L from the left lead into the QD in zone 0, as the chemical potential in the right lead is larger than the chemical potential in the left lead. In this zone, the system exhibits roughly sinusoidal oscillations.

If the chemical potential is increased beyond μ_{01}, the system shows non-sinusoidal oscillations (zone 1). The frequency of these oscillations decreases starkly as a function of the chemical potential.

At $\mu = \mu_{12}$, the frequency of oscillations has decreased strongly, the remaining, nearly square oscillations show a period several orders of magnitude longer than at $\mu = 0$.

If μ is increased further, attractive stationary states $\mathbf{P}_{\text{I}++}$ and $\mathbf{P}_{\text{I}--}$ occur (zone 2), where $+$ and $-$ denote the signs of $\left\langle \hat{J}_x \right\rangle$ and $\left\langle \hat{J}_y \right\rangle$, respectively. These states vary as a function of

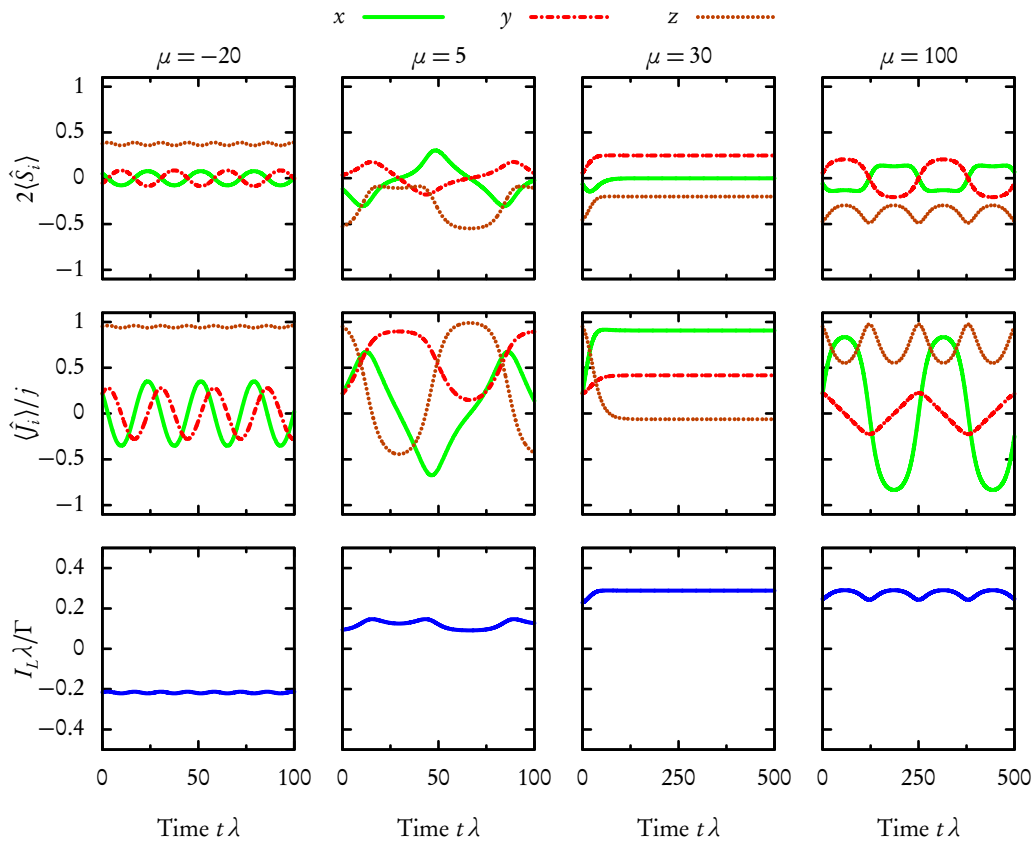

Figure 4: Behaviour in region I. We can identify four different zones (left to right: zone 0, 1, 2 and 3), each exhibiting a different behaviour of the system. Within zone 2, a different stationary state is attained if negative initial values for $\left\langle \hat{J}_x \right\rangle$ and $\left\langle \hat{J}_y \right\rangle$ are chosen. The initial values of $\left\langle \hat{J}_i \right\rangle$ were defined as follows: $\langle J_x(0) \rangle = \left\langle J_y(0) \right\rangle = (5/\sqrt{2})(\sqrt{5}-1)/2$, $\langle J_z(0) \rangle = (5/\sqrt{2})\sqrt{5+\sqrt{5}}$.

the potential μ (cf. Fig. 5); for $\mu \lesssim \mu_{23}$, a nearly complete polarisation, parallel to the x axis, is achieved.

Within zone 3, i.e. $\mu > \mu_{23}$, the system again shows oscillatory dynamics. The period of these oscillations decreases from very large values at $\mu \gtrsim \mu_{23}$ to finite values for $\mu \to \infty$ (cf. Fig. 3).

5.1.2. Fixed Points

To explain the transitions at μ_{01}, μ_{12} and μ_{23}, we analyse the fixed points of the system.

As seen in Section 4, at least two fixed points, $\mathbf{P}_{\pm}$, exist in region I. But in addition to these, we observe two more fixed points. They differ by the signs of the $\left\langle \hat{J}_{x,y} \right\rangle$ components; we introduced them as $\mathbf{P}_{\mathrm{I}++}$ and $\mathbf{P}_{\mathrm{I}--}$[3] above. By calculating the time-derivatives of $\left\langle \hat{J}_i \right\rangle$, we

[3] We will again use $\mathbf{P}_{\mathrm{I}}$ to refer to $\mathbf{P}_{\mathrm{I}++}$, $\mathbf{P}_{\mathrm{I}--}$, $\mathbf{P}_{\mathrm{I}+-}$ and $\mathbf{P}_{\mathrm{I}-+}$ collectively.

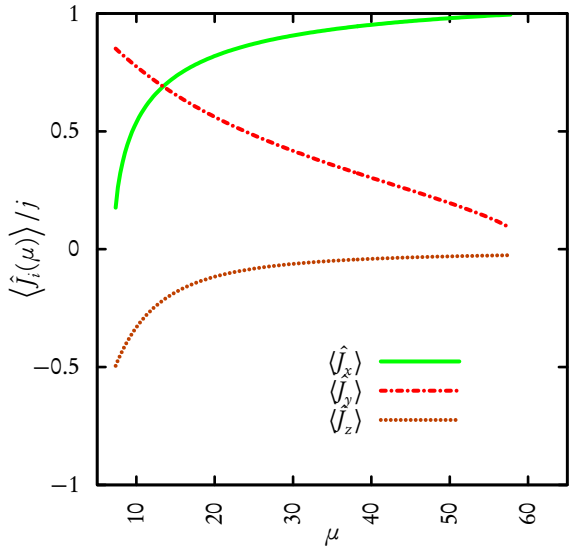

Figure 5: This plot shows the values of the components of $\langle \hat{J} \rangle$, $\langle \hat{J}_i \rangle$, at the stationary state $\mathbf{P}_{\mathrm{I}++}$ as a function of μ in zone 2 of region I. The value of the $\langle \hat{J}_y \rangle$ component decreases, while both the $\langle \hat{J}_x \rangle$ and $\langle \hat{J}_z \rangle$ component increase until a nearly complete polarisation, parallel to the x axis, is achieved.

can furthermore assert that two more, repulsive, fixed points exist, with the same absolute values of the $\langle \hat{J}_{x,y} \rangle$ components, but different signs: $\mathbf{P}_{\mathrm{I}+-}$ and $\mathbf{P}_{\mathrm{I}-+}$.

Moreover, we find that, by setting $\langle \hat{J}_x \rangle \equiv 0$, the equation

$$\langle \hat{S}_z \rangle \Big|_{\langle \hat{J}_x \rangle \equiv 0} + B_z = 0 \tag{5.1.1}$$

results in a value $\langle \hat{J}_z \rangle'$ that describes two other fixed points

$$\mathbf{P}_{\mathrm{X}\pm} = \left(0, \pm \sqrt{j^2 - \left(\langle \hat{J}_z \rangle' \right)^2}, \langle \hat{J}_z \rangle' \right), \tag{5.1.2}$$

which only differ in the signs of the $\langle \hat{J}_y \rangle$ component. Similarly to the infinite bias regime, all fixed points found here ($\mathbf{P}_{\mathrm{I}}$, $\mathbf{P}_{\mathrm{X}\pm}$) satisfy $\langle \hat{S}_z \rangle = -\frac{B_z}{\lambda}$ and $\langle \hat{S}_x \rangle = 0$.

The eigenvalues of the Jacobian of Eq. (2.3.3) – (2.3.5) in $\mathbf{P}_{\pm}$ and $\mathbf{P}_{\mathrm{X}\pm}$ can be calculated analytically (cf. Section A.4); one eigenvalue is always 0 because the system is essentially two-dimensional (due to the sum of $\langle \hat{J}_i \rangle^2$ being defined as j^2). The other two read

$$\mathscr{E}_{\mathbf{P}_\pm} = \pm i \sqrt{\langle \hat{S}_z \rangle + B_z} \sqrt{\langle \hat{S}_z \rangle + B_z - \langle \hat{J}_z \rangle \frac{\partial \langle \hat{S}_x \rangle}{\partial \langle \hat{J}_x \rangle}}, \tag{5.1.3}$$

$$\mathscr{E}_{\mathbf{P}_{\mathrm{X}\pm}} = \pm i \langle \hat{J}_y \rangle \sqrt{\frac{\partial \langle \hat{S}_x \rangle}{\partial \langle \hat{J}_x \rangle} \frac{\partial \langle \hat{S}_z \rangle}{\partial \langle \hat{J}_z \rangle}}. \tag{5.1.4}$$

Fig. 6a and 6b illustrate the eigenvalues of the Jacobian at $\mathbf{P}_{\pm}$ and $\mathbf{P}_{\mathrm{X}\pm}$ together with the values of $\pm \langle \hat{J}_y \rangle$ and $\langle \hat{J}_z \rangle'$ which solve equation Eq. (5.1.1). Using these figures, we can now

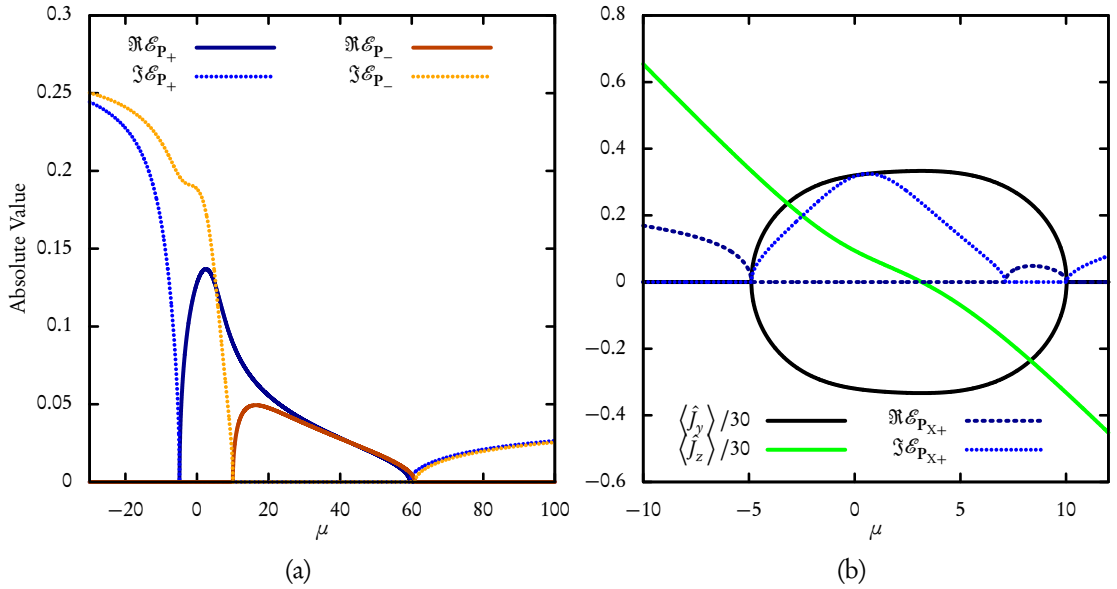

Figure 6: The eigenvalues of the Jacobian at $\mathbf{P}_\pm$ (a, left) and those of the Jacobian at $\mathbf{P}_{X\pm}$ (b, right) as a function of the potential μ in region I. The right plot also shows the corresponding values of $\langle\hat{J}_z\rangle'$ and possible values $\pm\langle\hat{J}_y\rangle$ at $\mathbf{P}_{X\pm}$.

identify all transitions between zones with changes in the eigenvalues of the Jacobian at $\mathbf{P}_{X\pm}$ or $\mathbf{P}_\pm$.

Furthermore, we are able to create a bifurcation diagram for region I, Fig. 7. It should be noted that this diagram (as well as Fig. 11) is only of qualitative, not quantitative, nature, since it is impossible to plot the two-dimensional system on a single ordinate.

Within zone 0, $\mathbf{P}_\pm$ are centres and therefore neutrally stable [27] with strictly imaginary eigenvalues (cf. Fig. 6a). The system exhibits sinusoidal oscillations (cf. Fig. 4).

At $\mu_{01} \approx -5$, $\mathbf{P}_+$ becomes a saddle point (hence loses stability) and solutions to Eq. (5.1.1) exist, namely $\mathbf{P}_{X\pm}$. From Fig. 6b, we can see that $\mathscr{E}_{\mathbf{P}_{X\pm}}$ are strictly imaginary in this zone; hence, $\mathbf{P}_{X\pm}$ are centres and neutrally stable. Furthermore, we note that, at this bias, $\langle\hat{J}_z\rangle' = 10$ (cf. $\langle\hat{J}_z\rangle$ in Fig. 6b). This implies that the new fixed points $\mathbf{P}_{X\pm}$ emerge directly at $\mathbf{P}_-$ at the moment when $\mathbf{P}_-$ loses stability. We can therefore classify this bifurcation as a supercritical pitchfork bifurcation [29], since one fixed point ($\mathbf{P}_-$) loses stability and two stable fixed points ($\mathbf{P}_{X\pm}$) emerge.

In zone 1, the system still shows oscillations due to the three centres $\mathbf{P}_-$ and $\mathbf{P}_{X\pm}$. However, the bifurcation at $\mathbf{P}_+$ leads to non-sinusoidal dynamics, since the vector field given by $\left(\langle\dot{\hat{J}}_x\rangle, \langle\dot{\hat{J}}_y\rangle, \langle\dot{\hat{J}}_z\rangle\right)$, defined on the sphere described by $r^2 = \langle\hat{J}\rangle^2$, is not governed by two opposing centres at each $\langle\hat{J}_z\rangle$ pole of the sphere but by three centres and one saddle point. From Fig. 6b, we see that $\mathbf{P}_{X\pm}$ move towards $\mathbf{P}_-$ on the great circle defined by $\langle\hat{J}_x\rangle = 0$, if the bias is increased.

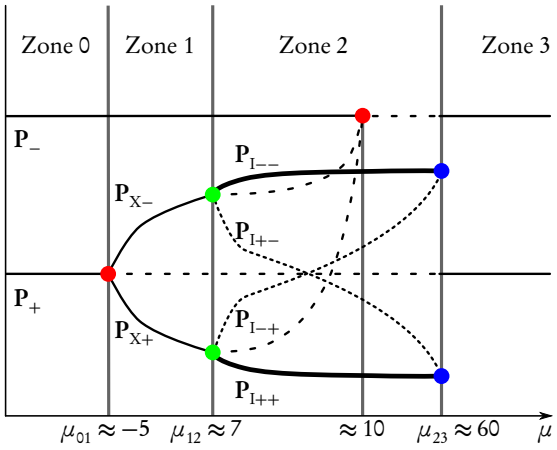

Figure 7: The effective bifurcation diagram for region I. Two pitchfork bifurcations (red dots), two imperfect pitchfork bifurcations (green) and two blue sky bifurcations (blue) are visible. Solid lines denote centres, bold solid lines attractive nodes, dashed lines saddle points and dotted lines repulsive nodes. Due to the two-dimensional nature of the system, the diagram only carries qualitative, not quantitative, meaning; the ordinate contains all three dimensions x, y, z.

The transition to zone 2 occurs at $\mu = \mu_{12} \approx 7.2$. Both formerly stable points $\mathbf{P}_{\mathrm{X}\pm}$ in each of the $\langle \hat{J}_y \rangle$ hemispheres lose stability at this potential (Fig. 6b). Additionally, we observe the creation of one attractive and one repulsive fixed point in each hemisphere, $\mathbf{P}_{++}$ and $\mathbf{P}_{-+}$ in the hemisphere described by $\langle \hat{J}_y \rangle > 0$. Exactly at $\mu = \mu_{12}$, these attractive fixed points coincide with $\mathbf{P}_{\mathrm{X}\pm}$ (cf. Fig. 5, Fig. 6b). But since one attractive and one repulsive node emerge from a centre, it is neither possible to classify this pitchfork bifurcation as supercritical nor subcritical. [27] suggests the classification as an imperfect pitchfork bifurcation.

Zone 2 is split into two parts: With $\mu_{12} < \mu \lesssim 10$, three saddle points ($\mathbf{P}_+$, $\mathbf{P}_{\mathrm{X}\pm}$) and one centre ($\mathbf{P}_-$) exist, apart from the attractive and repulsive nodes. If the applied bias is increased, the solution to Eq. (5.1.1) becomes inaccessible to the system, since the required value of $\langle \hat{J}_z \rangle'$ exceeds $|j|$, and the eigenvalues of the Jacobian at $\mathbf{P}_-$ become strictly real. Since $\mathbf{P}_-$ loses stability at this point and the two saddle points $\mathbf{P}_{\mathrm{X}\pm}$ vanish, this bifurcation is a subcritical pitchfork bifurcation [27]. The system then contains two saddle points ($\mathbf{P}_\pm$), two attractive nodes ($\mathbf{P}_{\mathrm{I}++}, \mathbf{P}_{\mathrm{I}--}$) and two repulsive nodes ($\mathbf{P}_{\mathrm{I}-+}, \mathbf{P}_{\mathrm{I}+-}$).

At $\mu = \mu_{23}$, the attractive and repulsive fixed points are polarised (anti-)parallel to the x axis. Then the two nodes with the same sign in the $\langle \hat{J}_x \rangle$ component collide, namely $\mathbf{P}_{\mathrm{I}++}$ with $\mathbf{P}_{\mathrm{I}+-}$ and $\mathbf{P}_{\mathrm{I}--}$ with $\mathbf{P}_{\mathrm{I}-+}$. For $\mu > \mu_{23}$, no such nodes exist, hence, blue sky bifurcations occur here. Furthermore, $\mathbf{P}_\pm$ regain stability with strictly imaginary eigenvalues (cf. Fig. 6a).

In zone 3, the two centres $\mathbf{P}_\pm$ are the only fixed points. The eigenvalues of the Jacobian at these points are imaginary and approach the corresponding values in the infinite bias regime smoothly and monotonously, starting at 0; the period of the oscillations slowly decreases, reversing the process that happened at $\mu \leq \mu_{12}$.

5.2. Region II

Region II supplements region I in the requirement that $B_z < \frac{\lambda}{4}$, but is otherwise characterised by low tunnelling rates. As previously noted, we concentrate on one set of parameters in region II, namely $B_z \equiv 0.2\lambda$, $\Gamma \equiv 0.7\lambda$.

5.2.1. Dynamics of the System

Fig. 8 illustrates the behaviour in region II, where we, again, treat μ as the sole parameter. Analogous to region I, it is possible to identify three zones with boundaries $\mu_{01} \approx -5$ and $\mu_{12} \approx 1.5$, respectively.

In zone 0, at very small/negative values of μ, the system exhibits sinusoidal oscillations. Since $\mu < 0$, the current I_L from the left lead into the QD is negative, as we expected.

When the applied bias is increased above μ_{01}, the system enters zone 1 and shows non-sinusoidal, but periodic, oscillations. While zone 0 and zone 1 are, in general, very similar to

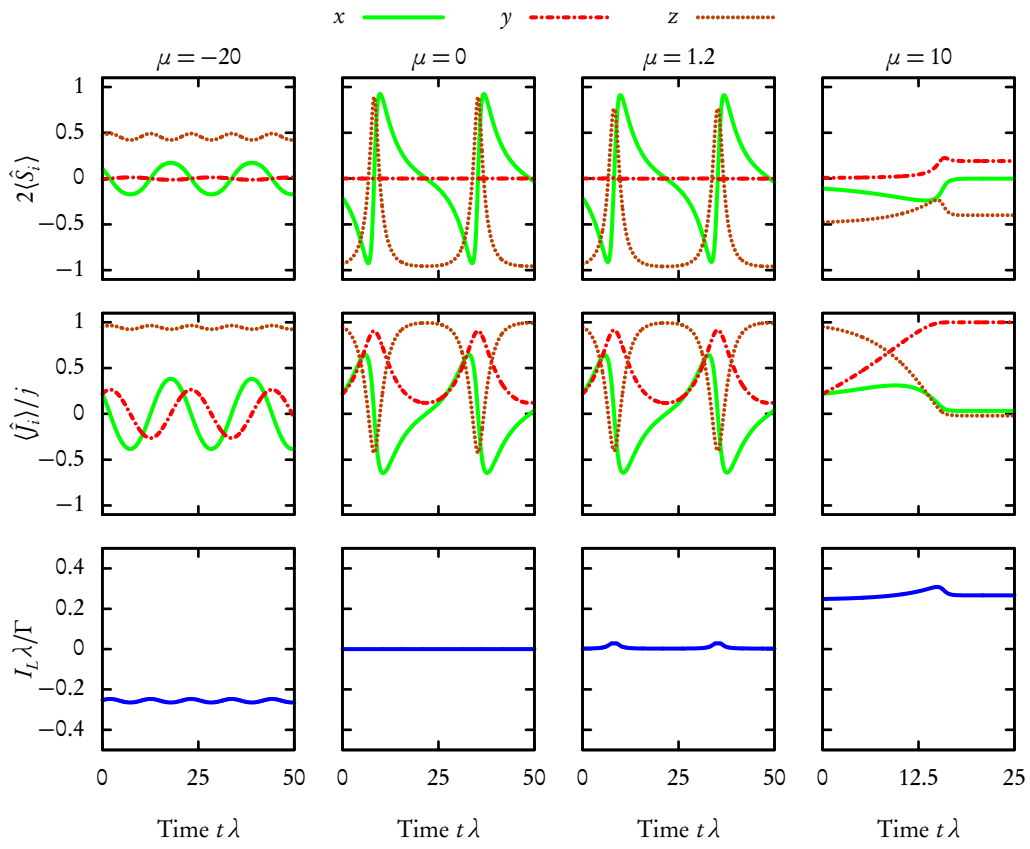

Figure 8: Dynamics in region II. It is possible to identify three zones: zone 0 with sinusoidal oscillations (left), zone 1 with non-sinusoidal oscillations (centre left and centre right) and zone 2, where the systems quickly enter stationary states. The initial values of $\left\langle \hat{J}_i \right\rangle$ were defined as follows: $\langle J_x(0)\rangle = \left\langle J_y(0) \right\rangle = (5/\sqrt{2})(\sqrt{5}-1)/2$, $\langle J_z(0)\rangle = (5/\sqrt{2})\sqrt{5+\sqrt{5}}$.

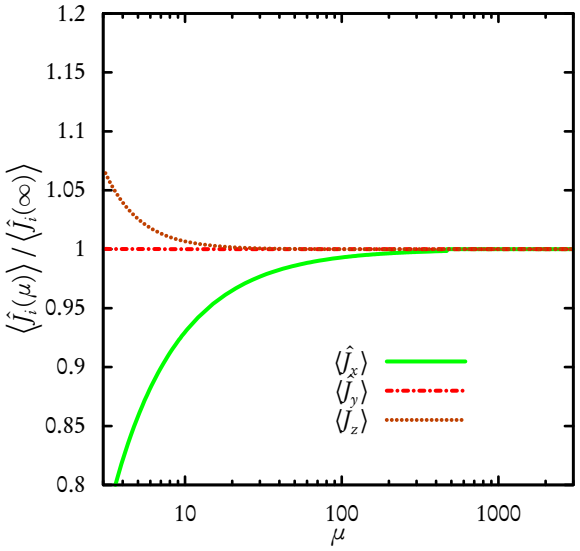

Figure 9: By normalising the large spin components $\langle \hat{J}_i \rangle$ at $\widetilde{\mathbf{P}}_{\mathrm{II}++}$ by the large spin components at the infinite bias fixed point $\mathbf{P}_{\mathrm{II}++}$, this plot illustrates the smooth and monotone convergence $\widetilde{\mathbf{P}}_{\mathrm{II}++} \to \mathbf{P}_{\mathrm{II}++}$ in region II.

their counterparts in region I, we observe a nearly constant frequency of oscillations in this zone.

Finally, if $\mu > \mu_{12}$, the system quickly enters a stationary state. Similar to region I, two attractive ($\widetilde{\mathbf{P}}_{\mathrm{II}++}, \widetilde{\mathbf{P}}_{\mathrm{II}--}$) and two repulsive ($\widetilde{\mathbf{P}}_{\mathrm{II}+-}, \widetilde{\mathbf{P}}_{\mathrm{II}-+}$) nodes exist. Identical to region I, the signs indicate the respective signs of the $\langle \hat{J}_x \rangle$ and $\langle \hat{J}_y \rangle$ components.

Fig. 9 illustrates the behaviour of $\widetilde{\mathbf{P}}_{\mathrm{II}++}$ as a function of the bias. It is visible that the attractive and repulsive nodes in region II converge on the infinite bias manifestations $\mathbf{P}_{\mathrm{II}}$, contrary to the dynamics in region I.

5.2.2. Fixed Points

To further understand this system, it is helpful to analyse the fixed points. Since Eq. (5.1.3) and Eq. (5.1.4) are still valid, we expect μ_{01} and μ_{12} to coincide with one of the zero points of $\mathscr{E}_{\mathbf{P}_+}$ and $\mathscr{E}_{\mathbf{P}_{\mathrm{X}\pm}}$, respectively.

Fig. 10a and Fig. 10b show the plots of these functions. With this information, we are again able to compile an effective bifurcation diagram, Fig. 11.

As we can see, $\mu_{01} \approx -5$ indeed correlates nicely with the root of $\mathscr{E}_{\mathbf{P}_+}$ and $\mathbf{P}_{\mathrm{X}\pm}$ is a centre in zone 1 (exactly as in region I). At this point a supercritical pitchfork bifurcation [27] takes place, as $\mathbf{P}_+$ loses its stability and $\mathbf{P}_{\mathrm{X}\pm}$ (centres, cf. Fig. 10b) become physically possible solutions. As in region I, $\mathbf{P}_{\mathrm{X}\pm}$ move on the great circle defined by $\langle \hat{J}_x \rangle = 0$ from $\mathbf{P}_+$ towards $\mathbf{P}_-$.

If $\mu = \mu_{12} \approx 1.5$, the same imperfect pitchfork bifurcations [27] as in region I take place, and spawn two attractive ($\widetilde{\mathbf{P}}_{\mathrm{II}++}, \widetilde{\mathbf{P}}_{\mathrm{II}--}$) and two repulsive ($\widetilde{\mathbf{P}}_{\mathrm{II}-+}, \widetilde{\mathbf{P}}_{\mathrm{II}+-}$) fixed points from $\mathbf{P}_{\mathrm{X}\pm}$, which then act as saddle points (cf. Fig 10b). These fixed points also fulfil the requirements $\langle \hat{S}_z \rangle = -\frac{B_z}{\lambda}$ and $\langle \hat{S}_x \rangle = 0$.

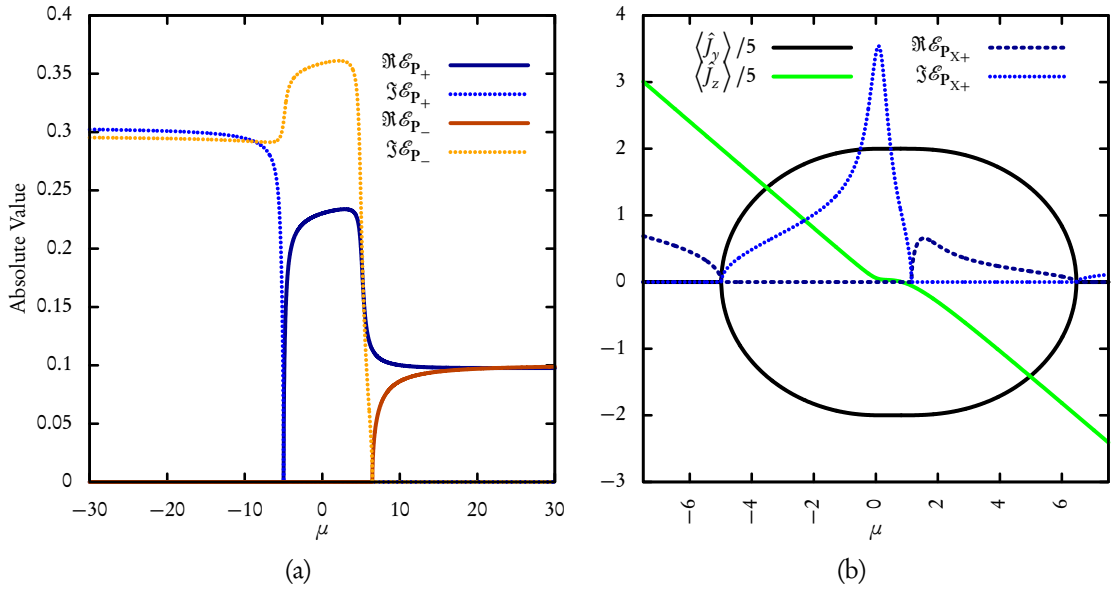

Figure 10: The eigenvalues of the Jacobian at $\mathbf{P}_{\pm}$ (a, left) and those of the Jacobian at $\mathbf{P}_{\mathrm{X}\pm}$ (b, right) as a function of the potential μ in region II. The right plot also illustrates the corresponding values of $\left\langle \hat{J}_z \right\rangle'$ and the possible values $\pm \left\langle \hat{J}_y \right\rangle$ at $\mathbf{P}_{\mathrm{X}\pm}$.

At $\mu \approx 7$, $\mathbf{P}_-$ also loses stability when it collides with the (unstable) saddle points $\mathbf{P}_{\mathrm{X}\pm}$; a subcritical pitchfork bifurcation occurs here [29], again exactly as in region I.

It is hence to be expected that there is a strong similarity between Fig. 11 and the bifurcation diagram for region I (Fig. 7), except for the blue sky bifurcations occurring in region I.

Apart from these correlations between μ_{01}, μ_{12} and the various roots of $\mathscr{E}$, we find that the imaginary part of $\mathscr{E}_{\mathbf{P}_+}$ is nearly constant in zone 1 (cf. Fig. 10a), compared to the sharp decrease in zone 1 of region I (cf. Fig. 6a). This explains the roughly constant frequency in zone 1 of region II compared to the frequency of oscillations in zone 1 of region I, which decreases as a function of μ.

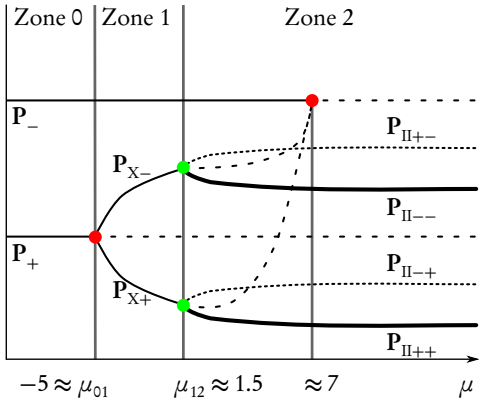

Figure 11: The effective bifurcation diagram for region II. As in region I, two pitchfork (red dots) and two imperfect pitchfork bifurcations (green) occur, but since $\mathbf{P}_{\mathrm{II}}$ also exist in the infinite bias regime, no Blue Sky bifurcations take place. Solid lines denote centres, bold solid lines attractive nodes, dashed lines saddle points and dotted lines repulsive nodes. As previously, only qualitative, not quantitative meaning is transported here, as the ordinate entails all three components $\left\langle \hat{J}_i \right\rangle$.

5.3. Region III

Region III is characterised by a very strong magnetic field. We set $B_z \equiv \lambda$ and $\Gamma \equiv 10\lambda$.

5.3.1. Dynamics of the System

Fig. 12 shows the dynamics of a system in region III. No major changes in oscillation frequency, stationary states, etc. take place. Only small changes are visible for small values of $|\mu|$: $\left\langle \hat{J}_z \right\rangle$ starts to oscillate slightly, and electron spin oscillations are dominated by the $\left\langle \hat{S}_x \right\rangle$ component rather than the $\left\langle \hat{S}_y \right\rangle$ component. Additionally, the symmetry between positive and negative values of μ is very strong; $\mu = -20$ and $\mu = 20$ only differ by a slightly lower frequency in oscillations and a reversed current.

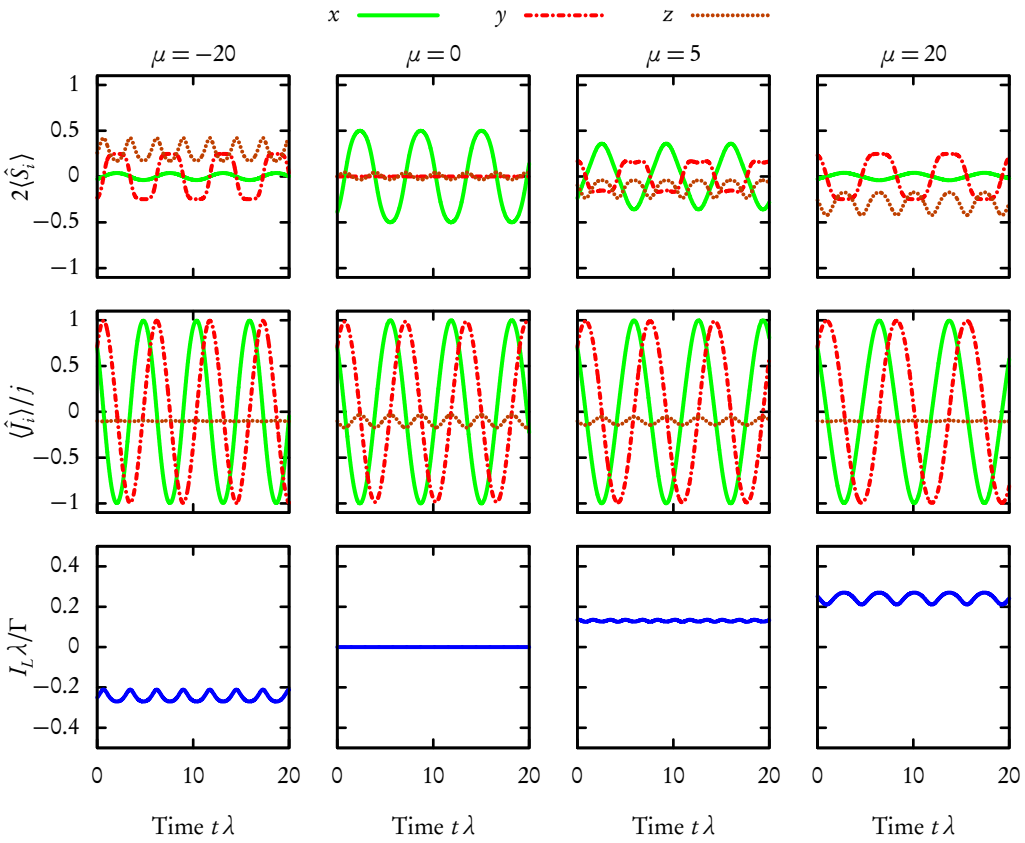

Figure 12: Dynamics in region III. No major changes occur as the bias is increased, and the system always shows nearly-sinusoidal oscillations, except for stronger oscillations of $\left\langle \hat{J}_z \right\rangle$ if $|\mu|$ is small. Initial values as follows: $\left\langle \hat{J}_x(0) \right\rangle = \left\langle \hat{J}_y(0) \right\rangle = 3\sqrt{6.5}$, $\left\langle \hat{J}_z(0) \right\rangle = -1$.

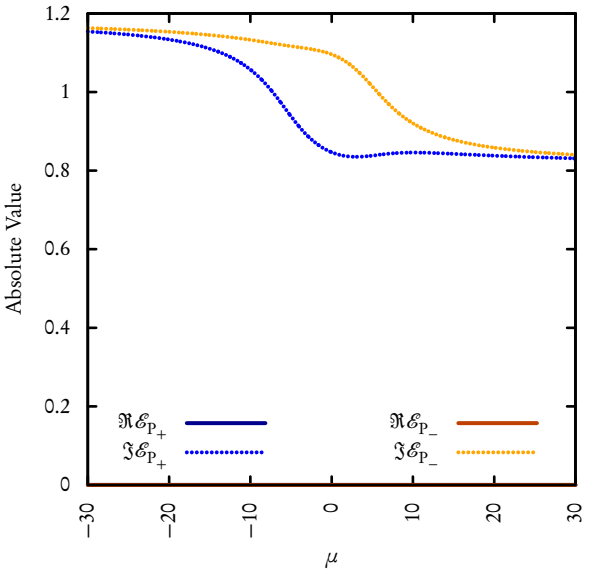

Figure 13: $\mathscr{E}_{\mathbf{P}_\pm}$ plotted as a function of the potential μ in region III. There are no zero points in this case and the eigenvalues are always entirely imaginary, but for very small values of $|\mu|$, a difference between $\mathscr{E}_{\mathbf{P}+}$ and $\mathscr{E}_{\mathbf{P}-}$ emerges, which explains the slightly different oscillations for such values of μ (cf. Fig. 12).

5.3.2. Fixed Points

Contrary to the dynamics in region I and II, Eq. (5.1.1) does not have solutions in region III. Additionally, as can be seen from Fig. 13, the eigenvalues of the Jacobian at $\mathbf{P}_\pm$ are always entirely imaginary.

But with the help of Fig. 13, we are able to explain the drop in frequency observed in Fig. 12 between $\mu = -20$ and $\mu = 20$. First, we note that the frequency of the oscillations in Fig. 12 are, assuming dimensionless units, approximately 0.36 at $\mu = -20$ and 0.29 at $\mu = 20$. These values have been obtained from a Fourier transformation of the $\left\langle \hat{J}_x \right\rangle$ component.

Second, we recall that the imaginary parts of the eigenvalues of the Jacobian at a centre are first-order estimates for the velocity of a point on an orbital path around the centre. Hence, the ratio of eigenvalues of the Jacobian at the centres at different potentials can act as a (very rough) approximation for the ratio of oscillation frequency at those potentials:

$$\frac{3}{4} \approx \frac{0.36}{0.29} = \frac{\nu(20)}{\nu(-20)} \approx \frac{\mathscr{E}_{\mathbf{P}_\pm}(20)}{\mathscr{E}_{\mathbf{P}_\pm}(-20)} = \frac{0.83i}{1.15i} \approx \frac{3}{4}, \tag{5.3.1}$$

where $\nu(\mu)$ denotes the frequency at potential μ. Numeric values for the eigenvalues were calculated from Eq. (5.1.3).

5.4. $\mathscr{A}$ and $\mathscr{B}$ in the Finite Bias Regime

To conclude the discussion of the finite bias regime, we recall Fig. 2 and the expressions for $\mathscr{A}$ and $\mathscr{B}$ (Eq. (4.1.5), (4.1.6)), which are per se only valid in the infinite bias regime. These expressions inflict two restrictions ($\mathfrak{R}_{\mathscr{A}}$ and $\mathfrak{R}_{\mathscr{B}}$) on B_z/λ and Γ/λ. They are equivalent to the requirements fulfilled by (nearly) all fixed points, $\left\langle \hat{S}_z \right\rangle = -\frac{B_z}{\lambda}$ and $\left\langle \hat{S}_x \right\rangle = 0$. In region I, $\mathfrak{R}_{\mathscr{A}}$ is fulfilled, while $\mathfrak{R}_{\mathscr{B}}$ is violated; region III violates $\mathfrak{R}_{\mathscr{A}}$, but fulfils $\mathfrak{R}_{\mathscr{B}}$.

Since we observe attractive fixed points in the finite bias regime in region I, but not in region III, it appears plausible to assume that the finite bias affects $\mathfrak{R}_{\mathscr{B}}$, but not $\mathfrak{R}_{\mathscr{A}}$, resulting in attractive fixed points in region I. Furthermore, this suggests a close relationship between the nodes $\mathbf{P}_{\mathrm{I}}$ and $\mathbf{P}_{\mathrm{II}}$, which is supported by the similarity in the occurring bifurcations causing these fixed points and the values attained by $\left\langle \hat{S}_x \right\rangle$ and $\left\langle \hat{S}_z \right\rangle$ at the fixed points.

However, a closer inspection of this effect would require analytic expressions for Eq. (2.3.3) – (2.3.5) with analytic roots, or at least analytic expressions for $\widetilde{\mathbf{P}}_{\mathrm{II}}$ and $\mathbf{P}_{\mathrm{I}}$ in the finite bias regime. The currently known expressions in terms of arctan() for $\left\langle \hat{S}_i \right\rangle$ do not satisfy this requirement.

6. Conclusion

This work used Keldysh Green's function and an adiabatic approach to describe tunnelling through a quantum dot. The achieved results match previous results [1] in the infinite bias regime, especially if the system exhibits periodic, non-chaotic oscillations, while neither chaotic nor damped dynamics were reproduced here.

Nevertheless, the ability to systematically treat the finite bias regime allowed us to find attractive fixed points in region I, which are very similar to those in region II, but that do not occur in the infinite bias regime and were thus inaccessible to the equation of motion technique employed by [1]. It is hence necessary to refine the division of parameter space insofar as that region I and II are much closer related to each other than each of these and region III.

Furthermore, by comparing these results with those presented by [1], as well as current work [30] by A. Metelmann, we are able to show that the adiabatic approach used here helps with the analysis of the non-adiabatic finite bias regime, since the existence and stability of fixed points found in this work carries over to the non-adiabatic case, although crucial properties, such as chaotic or damped behaviour, are not visible here.

7. Acknowledgements

I would like to thank Anja Metelmann for guidance and clarificatory discussions as well as Andrew Blatchford for linguistic support. I furthermore acknowledge support from the Robert Bosch GmbH and the Bundesministerium für Bildung und Forschung as part of the Deutschlandstipendium.

A. Appendix

A.1. Mean-Field-Approximation

Assume that $\hat{J}_i$ is very large and can be written as

$$\hat{J}_i = \left\langle \hat{J}_i \right\rangle + \delta \hat{J}_i, \tag{A.1.1}$$

with small fluctuations $\delta \hat{J}_i$. It then follows that:

$$\begin{aligned}
\hat{J}_i \hat{S}_i &= \left\langle \hat{J}_i \right\rangle \left\langle \hat{S}_i \right\rangle + \left\langle \hat{S}_i \right\rangle \delta \hat{J}_i + \left\langle \hat{J}_i \right\rangle \delta \hat{S}_i + \delta \hat{S}_i \delta \hat{J}_i && \text{(A.1.2)} \\
&\approx \left\langle \hat{J}_i \right\rangle \left\langle \hat{S}_i \right\rangle + \left\langle \hat{S}_i \right\rangle \delta \hat{J}_i + \left\langle \hat{J}_i \right\rangle \delta \hat{S}_i && \text{(A.1.3)} \\
&= \left\langle \hat{J}_i \right\rangle \left\langle \hat{S}_i \right\rangle + \left\langle \hat{S}_i \right\rangle \left(\hat{J}_i - \left\langle \hat{J}_i \right\rangle \right) + \left\langle \hat{J}_i \right\rangle \left(\hat{S}_i - \left\langle \hat{S}_i \right\rangle \right) && \text{(A.1.4)} \\
&= \left\langle \hat{S}_i \right\rangle \hat{J}_i + \left\langle \hat{J}_i \right\rangle \hat{S}_i - \langle J_i \rangle \langle S_i \rangle . && \text{(A.1.5)}
\end{aligned}$$

A.2. Equations of Motion

To calculate $\left[\hat{J}_k, \hat{H}^{\mathrm{MF}}\right]$, it is convenient to examine the three summands independently:

$$\begin{aligned}
\left[\hat{J}_k, \hat{H}_{\mathrm{FA}}\right] &= 0, && \text{(A.2.1)} \\
\left[\hat{J}_k, \hat{H}_{SJ}^{\mathrm{MF}}\right] &= \left[J_k, \sum_{l=x,z} \lambda \left(\hat{S}_l \left\langle \hat{J}_l \right\rangle + \left\langle \hat{S}_l \right\rangle \hat{J}_l - \left\langle \hat{S}_l \right\rangle \left\langle \hat{J}_l \right\rangle \right) \right] && \text{(A.2.2)} \\
&= \sum_{l=x,z} \lambda \left(\hat{J}_k \left\langle \hat{S}_l \right\rangle \hat{J}_l - \left\langle \hat{S}_l \right\rangle \hat{J}_l \hat{J}_k \right) && \text{(A.2.3)} \\
&= \sum_{l=x,z} \lambda \left\langle \hat{S}_l \right\rangle \left[\hat{J}_k, \hat{J}_l\right] && \text{(A.2.4)} \\
&= \lambda \left(\left\langle \hat{S}_x \right\rangle \left[\hat{J}_k, \hat{J}_x\right] + \left\langle \hat{S}_z \right\rangle \left[\hat{J}_k, \hat{J}_z\right] \right), && \text{(A.2.5)} \\
\left[\hat{J}_k, \hat{H}_J\right] &= B_z \left[\hat{J}_k, \hat{J}_z\right] . && \text{(A.2.6)}
\end{aligned}$$

The equations of motion Eq. (2.3.3) – (2.3.5) directly follow using the canonical commutator relations [32] for angular momentum operators $\left[\hat{J}_k, \hat{J}_l\right] = i \varepsilon_{klm} \hat{J}_m$.

A.3. Derivation of the Dyson Equation (3.1.1)

To derive the Dyson equation (3.1.1), it is useful to calculate a few commutators and time derivatives which are necessary later on[4]:

$$\sum_{\tau} \left[d_\tau^\dagger d_\tau, d_\sigma \right] = -d_\sigma, \tag{A.3.1}$$

[4] In the following, β and α denote leads (L, R), τ and σ spins $(\uparrow, \downarrow)$ and l, k momentum/energy states in the leads. ε_σ is defined in Eq. (3.1.2).

$$\sum_{k\beta\tau}\left(V_{k\beta\tau}\left[c^{\dagger}_{k\beta\tau}d_{\tau},d_{\sigma}\right]+V^{\star}_{k\beta\tau}\left[d^{\dagger}_{\tau}c_{k\beta\tau},d_{\sigma}\right]\right)=-\sum_{\beta,k}V^{\star}_{k\beta\sigma}c_{k\beta\sigma}, \tag{A.3.2}$$

$$\sum_{k\beta\tau}\left(V_{k\beta\tau}\left[c^{\dagger}_{k\beta\tau}d_{\tau},c_{l\alpha\sigma}\right]+V^{\star}_{k\beta\tau}\left[d^{\dagger}_{\tau}c_{k\beta\tau},c_{l\alpha\sigma}\right]\right)=-V_{l\alpha\sigma}d_{\sigma}, \tag{A.3.3}$$

$$\dot{c}_{k\alpha\sigma}|_{V\equiv 0}=-i\left[c_{k\alpha\sigma},\hat{H}_{V\equiv 0}\right]=-i\varepsilon_{k\alpha\sigma}c_{k\alpha\sigma}, \tag{A.3.4}$$

$$\dot{c}_{k\alpha\sigma}=-i\left[c_{k\alpha\sigma},\hat{H}\right]=-i\left(\varepsilon_{k\alpha\sigma}c_{k\alpha\sigma}-V_{k\alpha\sigma}d_{\sigma}\right), \tag{A.3.5}$$

$$\dot{d}_{\sigma}=-i\left[d_{\sigma},\hat{H}\right]=-i\left(\sum_{\alpha,k}V^{\star}_{k\alpha\sigma}c_{k\alpha\sigma}+\varepsilon_{\sigma}d_{\sigma}+\frac{\lambda^2}{4}\left\langle\hat{J}_x\right\rangle^2 d_{-\sigma}\right). \tag{A.3.6}$$

A.3.1. Retarded Lead Green's Function g^R

Employing Eq. (A.3.4), the total derivative of $g^R_{k\alpha\sigma,l\beta\tau}(t)$ with regard to time can then be calculated as:

$$\frac{\mathrm{d}}{\mathrm{d}t}g^R_{k\alpha\sigma,l\beta\tau}(t)=-i\delta(t)\left\langle\left\{c_{k\alpha\sigma}(t),c^{\dagger}_{l\beta\tau}\right\}\right\rangle-i\theta(t)\left\langle\left\{\dot{c}_{k\alpha\sigma}(t),c^{\dagger}_{l\beta\tau}\right\}\right\rangle \tag{A.3.7}$$

$$=-i\delta(t)\delta_{\alpha,\beta}\delta_{\sigma,\tau}\delta(k-l)-i\varepsilon_{k\alpha\sigma}g^R_{k\alpha\sigma,l\beta\tau}(t), \tag{A.3.8}$$

$$g^R_{k\alpha\sigma,l\beta\tau}(\omega)=\frac{\delta(k-l)\delta_{\alpha\beta}\delta_{\sigma\tau}}{\omega-\varepsilon_{k\alpha\sigma}}. \tag{A.3.9}$$

Eq. (A.3.9) follows from Eq. (A.3.8) using the Heisenberg equation of motion for g^R and noting that g^R commutes with $\hat{H}$, followed by a Fourier transformation.

A.3.2. Retarded Tunnelling Green's Function $G^R_{k\alpha\sigma,\tau}$

A similar approach to above, using Eq. (A.3.5) instead of Eq. (A.3.4) in conjunction with definition Eq. (3.0.8), leads to the following equation for $G^R_{k\alpha\sigma,\tau}$:

$$-i\varepsilon_{k\alpha\sigma}G^R_{k\alpha\sigma,\tau}(t)-iV_{k\alpha\sigma}G^R_{\sigma,\tau}(t)=G^R_{k\alpha\sigma,\tau}(t), \tag{A.3.10}$$

which, after a Fourier transformation, yields:

$$g^R_{k\alpha\sigma,k\alpha\sigma}(t)V_{k\alpha\sigma}G^R_{\sigma,\tau}(\omega)=G^R_{k\alpha\sigma,\tau}(\omega). \tag{A.3.11}$$

A.3.3. Retarded Dot Green's Function $G^R_{\sigma,\tau}$

Calculating the time derivative of d_σ, as given by Eq. (A.3.6), and the total time derivative of $G^R_{\sigma,\tau}$ results in the following equation:

$$\left(i\partial_t - \varepsilon_\sigma\right) G^R_{\sigma,\tau}(t) - \frac{\lambda\left\langle \hat{J}_x\right\rangle}{2} G^R_{-\sigma,\tau}(t) - \sum_{\alpha,k} V^\star_{k\alpha\sigma} G^R_{k\alpha\sigma,\tau}(t) = \delta(t)\delta_{\sigma,\tau}. \tag{A.3.12}$$

After applying a Fourier transform, inserting Eq. (A.3.11) leads to Eq. (3.1.1). Solving this equation leads to these expressions for $G^R_{\sigma,\tau}(\omega)$:

$$G^R_{\uparrow,\uparrow}(\omega) = \frac{\omega + \varepsilon_\uparrow + \Gamma_\downarrow}{(\omega+\varepsilon_\uparrow+\Gamma_\downarrow)(\omega+\varepsilon_\downarrow+\Gamma_\uparrow) - \frac{\lambda^2}{4}\left\langle \hat{J}_x\right\rangle^2}, \tag{A.3.13}$$

$$G^R_{\downarrow,\uparrow}(\omega) = \frac{\frac{\lambda}{2}\left\langle \hat{J}_x\right\rangle}{(\omega+\varepsilon_\uparrow+\Gamma_\downarrow)(\omega+\varepsilon_\downarrow+\Gamma_\uparrow) - \frac{\lambda^2}{4}\left\langle \hat{J}_x\right\rangle^2}, \tag{A.3.14}$$

$$G^R_{\downarrow,\downarrow}(\omega) = \frac{\omega + \varepsilon_\downarrow + \Gamma_\uparrow}{(\omega+\varepsilon_\uparrow+\Gamma_\downarrow)(\omega+\varepsilon_\downarrow+\Gamma_\uparrow) - \frac{\lambda^2}{4}\left\langle \hat{J}_x\right\rangle^2}, \tag{A.3.15}$$

$$G^R_{\uparrow,\downarrow}(\omega) = \frac{\frac{\lambda}{2}\left\langle \hat{J}_x\right\rangle}{(\omega+\varepsilon_\uparrow+\Gamma_\downarrow)(\omega+\varepsilon_\downarrow+\Gamma_\uparrow) - \frac{\lambda^2}{4}\left\langle \hat{J}_x\right\rangle^2}, \tag{A.3.16}$$

A.3.4. Lesser Dot Green's Function $G^<_{\sigma,\tau}$

When evaluating Eq. (3.2.2), it is helpful to remember that $\boldsymbol{G}^R$ is symmetric and hence $\boldsymbol{G}^A = (\boldsymbol{G}^R)^\star$. Therefore, the general expression for $\boldsymbol{G}^<$ is:

$$\boldsymbol{G}^< = \begin{pmatrix} \left|G^R_{\uparrow,\uparrow}\right|^2\Sigma^<_\uparrow + \left|G^R_{\uparrow,\downarrow}\right|^2\Sigma^<_\downarrow & \Sigma^<_\uparrow G^R_{\uparrow,\uparrow}G^A_{\uparrow,\downarrow} + \Sigma^<_\downarrow G^A_{\downarrow,\downarrow}G^R_{\uparrow,\downarrow} \\ \Sigma^<_\uparrow G^A_{\uparrow,\uparrow}G^R_{\uparrow,\downarrow} + \Sigma^<_\downarrow G^R_{\downarrow,\downarrow}G^A_{\uparrow,\downarrow} & \left|G^R_{\uparrow,\downarrow}\right|^2\Sigma^<_\uparrow + \left|G^R_{\downarrow,\downarrow}\right|^2\Sigma^<_\downarrow \end{pmatrix}. \tag{A.3.17}$$

We can then use

$$\left\langle \hat{S}_x\right\rangle = \frac{-i}{2}\int \frac{\mathrm{d}\omega}{2\pi}(G^<_{\downarrow,\uparrow}(\omega) + G^<_{\uparrow,\downarrow}(\omega)), \tag{A.3.18}$$

$$\left\langle \hat{S}_y\right\rangle = \frac{-1}{2}\int \frac{\mathrm{d}\omega}{2\pi}(G^<_{\downarrow,\uparrow}(\omega) - G^<_{\uparrow,\downarrow}(\omega)), \tag{A.3.19}$$

$$\left\langle \hat{S}_z\right\rangle = \frac{-i}{2}\int \frac{\mathrm{d}\omega}{2\pi}(G^<_{\uparrow,\uparrow}(\omega) - G^<_{\downarrow,\downarrow}(\omega)) \tag{A.3.20}$$

to calculate $\left\langle \hat{S}_i\right\rangle$.

An exemplary analytic expression for $\left\langle \hat{S}_z \right\rangle$ at $T \equiv 0$ reads:

$$\left\langle \hat{S}_z \right\rangle = \frac{1}{4\sqrt{\mathscr{Y}}\pi\left(\mathscr{Y}+\Gamma^2\right)} \Bigg\{ \left(\sqrt{\mathscr{Y}}+i\Gamma\right)\left(\sqrt{\mathscr{Y}}\Gamma+i\mathscr{X}\right) \operatorname{arctanh}\left(\frac{2\mu}{\sqrt{\mathscr{Y}}-i\Gamma}\right) \tag{A.3.21}$$

$$+\left(\sqrt{\mathscr{Y}}-i\Gamma\right)\left(\sqrt{\mathscr{Y}}\Gamma-i\mathscr{X}\right) \operatorname{arctanh}\left(\frac{2\mu}{\sqrt{\mathscr{Y}}+i\Gamma}\right)$$

$$+2\left(B_z+\left\langle \hat{J}_z \right\rangle\right)\left(\mathscr{Y}+\Gamma^2\right) \left(\begin{cases} -\pi+\arctan\left(\frac{2\sqrt{\mathscr{Y}}\,\mathrm{Abs}[\Gamma]}{\mathrm{Abs}\left[-\mathscr{Y}+\Gamma^2+4\mu^2\right]}\right) & \frac{\sqrt{\mathscr{Y}}\Gamma}{\mathscr{Y}-\Gamma^2-4\mu^2} \geq 0 \\ \arctan\left(\frac{2\sqrt{\mathscr{Y}}\Gamma}{\mathscr{Y}-\Gamma^2-4\mu^2}\right) & \text{otherwise} \end{cases} \right) \Bigg\},$$

where we used

$$\mathscr{X} \equiv \left(B_z+\left\langle \hat{J}_z \right\rangle\right)^2, \tag{A.3.22}$$

$$\mathscr{Y} \equiv \left\langle \hat{J}_x \right\rangle^2 + \mathscr{X}. \tag{A.3.23}$$

A.4. Analytic Expressions for Eigenvalues of Fixed Points

The general Jacobian of the system Eq. (2.3.3) – (2.3.5) is:

$$\mathbf{J} = \begin{pmatrix} -\frac{\partial\left\langle \hat{S}_z \right\rangle}{\partial\left\langle \hat{J}_x \right\rangle}\left\langle \hat{J}_y \right\rangle & -\mathscr{C} & -\frac{\partial\left\langle \hat{S}_z \right\rangle}{\partial\left\langle \hat{J}_z \right\rangle}\left\langle \hat{J}_y \right\rangle \\ \mathscr{C}+\frac{\partial\left\langle \hat{S}_z \right\rangle}{\partial\left\langle \hat{J}_x \right\rangle}\left\langle \hat{J}_x \right\rangle-\frac{\partial\left\langle \hat{S}_x \right\rangle}{\partial\left\langle \hat{J}_x \right\rangle}\left\langle \hat{J}_z \right\rangle & 0 & \frac{\partial\left\langle \hat{S}_z \right\rangle}{\partial\left\langle \hat{J}_z \right\rangle}\left\langle \hat{J}_x \right\rangle-\left\langle \hat{S}_x \right\rangle-\frac{\partial\left\langle \hat{S}_x \right\rangle}{\partial\left\langle \hat{J}_z \right\rangle}\left\langle \hat{J}_z \right\rangle \\ \frac{\partial\left\langle \hat{S}_x \right\rangle}{\partial\left\langle \hat{J}_x \right\rangle}\left\langle \hat{J}_y \right\rangle & \left\langle \hat{S}_x \right\rangle & \frac{\partial\left\langle \hat{S}_x \right\rangle}{\partial\left\langle \hat{J}_z \right\rangle}\left\langle \hat{J}_y \right\rangle \end{pmatrix}, \tag{A.4.1}$$

with

$$\mathscr{C} \equiv \left\langle \hat{S}_z \right\rangle + B_z \tag{A.4.2}$$

to shorten the notation.

We should note that $\frac{\partial\left\langle \hat{S}_x \right\rangle}{\partial\left\langle \hat{J}_z \right\rangle}$, $\left\langle \hat{S}_x \right\rangle$ and $\frac{\partial\left\langle \hat{S}_z \right\rangle}{\partial\left\langle \hat{J}_x \right\rangle}$ all sport terms proportional to $\left\langle \hat{J}_x \right\rangle$. Therefore, for $\left\langle \hat{J}_x \right\rangle \equiv 0$, $\mathbf{J}$ simplifies to:

$$\mathbf{J}_{\langle \hat{J}_x \rangle \equiv 0} = \begin{pmatrix} 0 & -\left(\left\langle \hat{S}_z \right\rangle + B_z\right) & -\frac{\partial\left\langle \hat{S}_z \right\rangle}{\partial\left\langle \hat{J}_z \right\rangle}\left\langle \hat{J}_y \right\rangle \\ -\frac{\partial\left\langle \hat{S}_x \right\rangle}{\partial\left\langle \hat{J}_x \right\rangle}\left\langle \hat{J}_z \right\rangle + \left\langle \hat{S}_z \right\rangle + B_z & 0 & 0 \\ \frac{\partial\left\langle \hat{S}_x \right\rangle}{\partial\left\langle \hat{J}_x \right\rangle}\left\langle \hat{J}_y \right\rangle & 0 & 0 \end{pmatrix}. \tag{A.4.3}$$

For $\mathbf{P}_{\pm}$, we have $\left\langle \hat{J}_y \right\rangle \equiv 0$, hence:

$$\mathbf{J}_{\mathbf{P}_{\pm}} = \begin{pmatrix} 0 & -\left(\left\langle \hat{S}_z \right\rangle + B_z\right) & 0 \\ -\frac{\partial \left\langle \hat{S}_x \right\rangle}{\partial \left\langle \hat{J}_x \right\rangle} \left\langle \hat{J}_z \right\rangle + \left\langle \hat{S}_z \right\rangle + B_z & 0 & 0 \\ 0 & 0 & 0 \end{pmatrix}. \tag{A.4.4}$$

The eigenvalues of $\mathbf{J}_{\mathbf{P}_{\pm}}$ are then given by Eq. (5.1.3).

Similarly, as above, but with $\left\langle \hat{J}_y \right\rangle \neq 0$, $\left\langle \hat{S}_z \right\rangle + B_z = 0$ (due to Eq. (5.1.1)), we have

$$\mathbf{J}_{\mathbf{P}_{\mathrm{X}\pm}} = \begin{pmatrix} 0 & 0 & -\frac{\partial \left\langle \hat{S}_z \right\rangle}{\partial \left\langle \hat{J}_z \right\rangle} \left\langle \hat{J}_y \right\rangle \\ -\frac{\partial \left\langle \hat{S}_x \right\rangle}{\partial \left\langle \hat{J}_x \right\rangle} \left\langle \hat{J}_z \right\rangle & 0 & 0 \\ \frac{\partial \left\langle \hat{S}_x \right\rangle}{\partial \left\langle \hat{J}_x \right\rangle} \left\langle \hat{J}_y \right\rangle & 0 & 0 \end{pmatrix}, \tag{A.4.5}$$

and the corresponding eigenvalues $\mathscr{E}_{\mathbf{P}_{\mathrm{X}\pm}}$ given by Eq. (5.1.4).

References

[1] Carlos López-Monís et al. 'Limit cycles and chaos in the current through a quantum dot'. In: *Phys. Rev. B* 85 (Jan. 2012), p. 045301. DOI: 10.1103/PhysRevB.85.045301.

[2] M. A. Reed et al. 'Observation of discrete electronic states in a zero-dimensional semiconductor nanostructure'. In: *Phys. Rev. Lett.* 60 (6 1988), pp. 535–537. DOI: 10.1103/PhysRevLett.60.535.

[3] R. Hanson et al. 'Spins in few-electron quantum dots'. In: *Rev. Mod. Phys.* 79 (4 2007), pp. 1217–1265. DOI: 10.1103/RevModPhys.79.1217.

[4] Toshimasa Fujisawa et al. 'Bidirectional Counting of Single Electrons'. In: *Science* 312.5780 (2006), pp. 1634–1636. DOI: 10.1126/science.1126788.

[5] Stephanie M. Reimann and Matti Manninen. 'Electronic structure of quantum dots'. In: *Rev. Mod. Phys.* 74 (4 2002), pp. 1283–1342. DOI: 10.1103/RevModPhys.74.1283. URL: http://link.aps.org/doi/10.1103/RevModPhys.74.1283.

[6] M. A. Reed et al. 'Conductance of a Molecular Junction'. In: *Science* 278.5336 (1997), pp. 252–254. DOI: 10.1126/science.278.5336.252.

[7] S Andergassen et al. 'Charge transport through single molecules, quantum dots and quantum wires'. In: *Nanotechnology* 21.27 (2010), p. 272001. DOI: 10.1088/0957-4484/21/27/272001.

[8] S. Gustavsson et al. 'Counting Statistics of Single Electron Transport in a Quantum Dot'. In: *Phys. Rev. Lett.* 96 (7 2006), p. 076605. DOI: 10.1103/PhysRevLett.96.076605.

[9] K. Ono et al. 'Current Rectification by Pauli Exclusion in a Weakly Coupled Double Quantum Dot System'. In: *Science* 297.5585 (2002), pp. 1313–1317. DOI: 10.1126/science.1070958.

[10] Gou Shinkai et al. 'Correlated Coherent Oscillations in Coupled Semiconductor Charge Qubits'. In: *Phys. Rev. Lett.* 103 (5 2009), p. 056802. DOI: 10.1103/PhysRevLett.103.056802.

[11] D. J. Reilly et al. 'Suppressing Spin Qubit Dephasing by Nuclear State Preparation'. In: *Science* 321.5890 (2008), pp. 817–821. DOI: 10.1126/science.1159221.

[12] Asher Peres. 'Ergodicity and mixing in quantum theory. I'. In: *Phys. Rev. A* 30 (1 1984), pp. 504–508. DOI: 10.1103/PhysRevA.30.504.

[13] Mario Feingold, Nimrod Moiseyev and Asher Peres. 'Ergodicity and mixing in quantum theory. II'. In: *Phys. Rev. A* 30 (1 1984), pp. 509–511. DOI: 10.1103/PhysRevA.30.509.

[14] E. Magyari et al. 'Integrable and nonintegrable classical spin clusters'. In: *Zeitschrift für Physik B Condensed Matter* 65 (3 1987). 10.1007/BF01303725, pp. 363–374. ISSN: 0722-3277. DOI: 10.1007/BF01303725.

[15] Daniel T. Robb and L. E. Reichl. 'Chaos in a two-spin system with applied magnetic field'. In: *Phys. Rev. E* 57 (2 1998), pp. 2458–2459. DOI: 10.1103/PhysRevE.57.2458.

[16] Keiji Ono and Seigo Tarucha. 'Nuclear-Spin-Induced Oscillatory Current in Spin-Blockaded Quantum Dots'. In: *Phys. Rev. Lett.* 92 (25 2004), p. 256803. DOI: 10.1103/PhysRevLett.92.256803.

[17] F. H. L. Koppens et al. 'Control and Detection of Singlet-Triplet Mixing in a Random Nuclear Field'. In: *Science* 309.5739 (2005), pp. 1346–1350. DOI: 10.1126/science.1113719.

[18] Carsten Timm and Florian Elste. 'Spin amplification, reading, and writing in transport through anisotropic magnetic molecules'. In: *Phys. Rev. B* 73 (23 2006), p. 235304. DOI: 10.1103/PhysRevB.73.235304.

[19] Moon-Ho Jo et al. 'Signatures of Molecular Magnetism in Single-Molecule Transport Spectroscopy'. In: *Nano Letters* 6.9 (2006), pp. 2014–2020. DOI: 10.1021/nl061212i.

[20] Niels Bode et al. 'Current-induced switching in transport through anisotropic magnetic molecules'. In: *Phys. Rev. B* 85 (11 2012), p. 115440. DOI: 10.1103/PhysRevB.85.115440.

[21] Hartmut J. W. Haug and Antti-Pekka Jauho. *Quantum Kinetics in Transport and Optics of Semiconductors*. 2nd ed. Berlin, Heidelberg, New York: Springer, 2008.

[22] U. Fano. 'Effects of Configuration Interaction on Intensities and Phase Shifts'. In: *Phys. Rev.* 124 (6 1961), pp. 1866–1878. DOI: 10.1103/PhysRev.124.1866.

[23] P. W. Anderson. 'Localized Magnetic States in Metals'. In: *Phys. Rev.* 124 (1 1961), pp. 41–53. DOI: 10.1103/PhysRev.124.41.

[24] J. Könemann et al. 'Spin-Orbit Coupling and Anisotropy of Spin Splitting in Quantum Dots'. In: *Phys. Rev. Lett.* 94 (22 2005), p. 226404. DOI: 10.1103/PhysRevLett.94.226404.

[25] Per Bak. 'Chaotic Behavior and Incommensurate Phases in the Anisotropic Ising Model with Competing Interactions'. In: *Phys. Rev. Lett.* 46 (13 1981), pp. 791–794. DOI: 10.1103/PhysRevLett.46.791.

[26] Toshifumi Futamase, Tony Rothman and Richard Matzner. 'Behavior of chaotic inflation in anisotropic cosmologies with nonminimal coupling'. In: *Phys. Rev. D* 39 (2 1989), pp. 405–411. DOI: 10.1103/PhysRevD.39.405.

[27] Steven H. Strogatz. *Nonlinear Dynamics and Chaos*. Reading, Massachusets: Perseus Books, 1994.

[28] John David Crawford. 'Introduction to bifurcation theory'. In: *Rev. Mod. Phys.* 63 (4 1991), pp. 991–1037. DOI: 10.1103/RevModPhys.63.991.

[29] Yuri A. Kuznetsov. *Elements of Applied Bifurcation Theory*. 2nd ed. Berlin, Heidelberg, New York: Springer, 1998.

[30] Anja Metelmann. 'Coherent Transport through Nanoelectromechanical Systems'. 2012.

[31] Clive Emary et al. 'Bunching and antibunching in electronic transport'. In: *Phys. Rev. B* 85 (16 2012), p. 165417. DOI: 10.1103/PhysRevB.85.165417.

[32] J. J. Sakurai. *Modern Quantum Mechanics Revised Edition*. Reading, Massachusets: Addison-Wesley, 1994.